Climate Dynamics (2020) 54:4711–4732
https://doi.org/10.1007/s00382-020-05249-8

Diagnosing the column-integrated moist static energy budget associated with the northward-propagating boreal summer intraseasonal oscillation

Tianyi Wang[1] · **Tim Li**[1]

Received: 16 December 2019 / Accepted: 15 April 2020 / Published online: 30 April 2020

Abstract
Column-integrated moist static energy (MSE) budgets associated with the northward-propagating boreal summer intraseasonal oscillation (BSISO) are diagnosed for the Bay of Bangel (BoB) and western North Pacific (WNP) regions. While an active BSISO convection is in phase with a positive column-integrated MSE perturbation, the MSE tendency exhibits a marked north–south asymmetry about the convection, with positive (negative) anomaly to its north (south). An MSE budget diagnosis reveals that the advection of anomalous MSE by the background southwesterly plays a dominant role in causing such an asymmetry and thus promotes the northward propagation, as the anomalous rainband associated with the BSISO has a northwest-southeast tilted structure. The anomalous BSISO wind plays a negative role, because the low-level easterly anomaly to the north of the BSISO convection tends to suppress the surface evaporation through reduced near-surface wind speed, inhibiting the north–south asymmetry. In addition, as maximum background MSE appears over the Asian land region, the advection by the low-level easterly anomaly contributes negatively over the WNP while it has little impact over the BoB. When the BSISO convection is near the equator, a much stronger subsidence anomaly appears to the north than the south due to the equatorial asymmetry of the summer mean state. This leads to a greater MSE tendency north of the equator due to greater anomalous vertical MSE advection, supporting the initiation of the northward propagation.

Keywords Boreal summer intraseasonal oscillation · Moist static energy budget · Northward propagation

1 Introduction

The tropical intraseasonal oscillation (ISO) exhibits pronounced seasonality in propagation (Madden 1986; Wang and Rui 1990; Madden and Julian 1994; Jones et al. 2004; Zhang and Dong 2004; Kikuchi et al. 2012; Adames et al. 2016) and initiation (Jiang and Li 2005; Wang et al. 2006; Zhao et al. 2013; Li et al. 2015). The typical boreal winter ISO, also known as the MJO (Madden and Julian 1971, 1972), is characterized by equatorially-trapped eastward-propagating convective anomalies, with a zonal wavenumber-1 structure and a principal period of 40–50 days (Salby and Hendon 1994; Hendon and Salby 1994). The boreal summer intraseasonal oscillation (BSISO) was firstly documented in the Asian summer monsoon in 1963 (Li et al. 2018). As shown in Fig. 1, the most outstanding contrasts between BSISO and winter MJO are the marked off-equatorial activities and northward propagations over the tropical Indian Ocean and western North Pacific during boreal summer (Yasunari 1979; Lau and Chan 1986; Wang and Rui 1990; Lawrence and Webster 2002; Jiang et al. 2004; Li and Wang 2005; Li 2014). In addition, a northwest-southeast tilted rainband is clearly identified in the BSISO of 30–60-day time scale (Wang et al. 2006; Lee et al. 2013). Another parallel mode of the BSISO, namely, the 10–20-day quasi-biweekly component (Krishnamurti and Ardanuy 1980; Chen and Chen 1993; Fukutomi and Yasunari 1999; Li and Wang 2005) is not intended to be investigated in this paper.

Various mechanisms have been proposed to understand the eastward propagation of MJO. Currently, the moisture mode theory is widely accepted, and there are two schools of thinking. One emphasizes the east–west moisture

✉ Tim Li
timli@hawaii.edu

[1] International Pacific Research Center and Department of Atmospheric Sciences, School of Ocean and Earth Science and Technology, University of Hawaii at Manoa, 1680 East West Road, POST Bldg. 401, Honolulu, HI 96822, USA

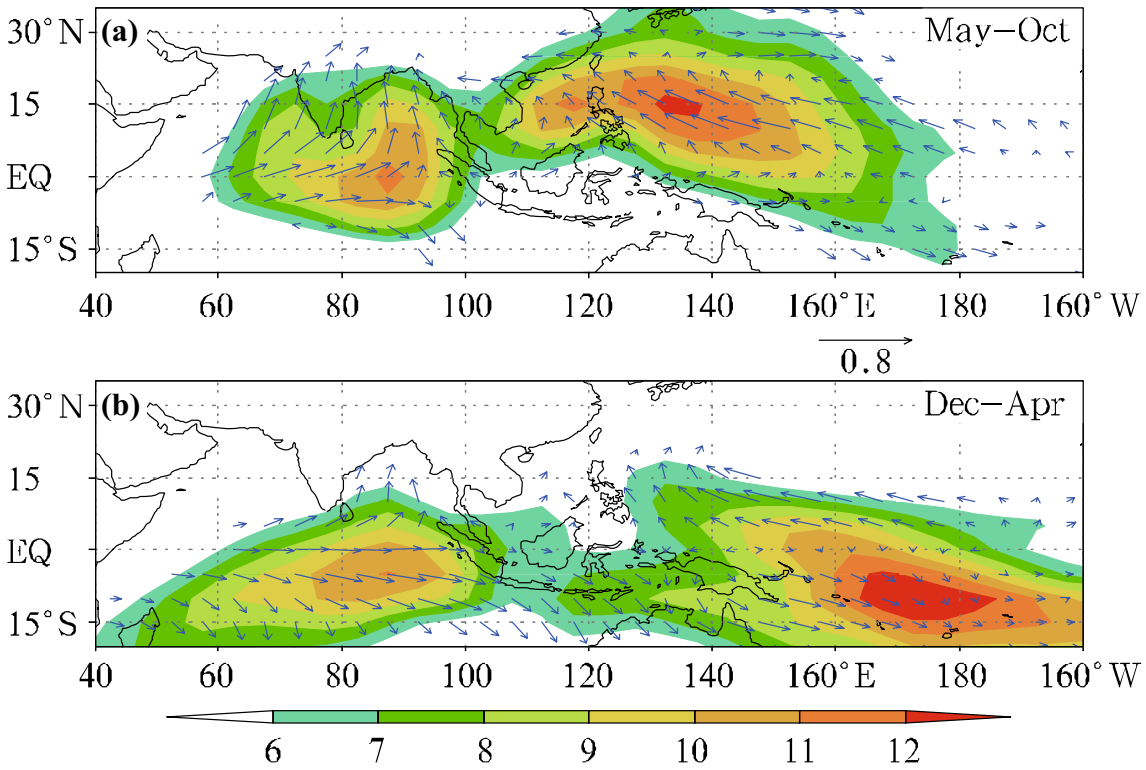

Fig. 1 The standard deviation of 20–80-day filtered CMAP rainfall anomalies (shaded, unit: mm/day) during 1979–1998 and propagation vectors for boreal **a** summer (May–October) and **b** winter (December–April). From Li (2014)

asymmetry in the planetary boundary layer (PBL) and its destabilizing effect (Hsu and Li 2012). The PBL moisture asymmetry is caused by the phase leading of PBL convergence (Wang and Li 1994; Hendon and Salby 1994), in which free-atmospheric wave dynamics play a dominant role, and air–sea interaction is partially responsible (Hsu and Li 2012; Cui et al. 2020). The other school of thinking excludes the PBL moistening effect but emphasizes the zonal asymmetry of column-integrated moist static energy (MSE) tendency, namely, the moisture mode theory (Raymond and Fuchs 2009; Sobel and Maloney 2012, 2013; Kim et al. 2014; Adames and Kim 2016). The zonal asymmetry of column-integrated MSE is primarily induced by horizontal MSE advection in lower-troposphere (Kim et al. 2014; Sobel et al. 2014; Adames and Wallace 2015; Jiang 2017) and vertical MSE advection in upper-troposphere associated with stratiform clouds (Wang et al. 2017; Wang and Li 2020). As illustrated in Wang et al. (2017), the advections of background MSE by the intraseasonal flow dominate in both horizontal and vertical directions.

The northward propagation of BSISO is generally explained with atmospheric internal dynamics and air–sea interactions. The former is mainly attributed to the interaction between convection-generated circulation and vertical shear of the background flow (Jiang et al. 2004; Drbohlav and Wang 2005; Tsou et al. 2005; Bellon and Sobel 2008a, b; Kang et al. 2010; Liu et al. 2015). In this vertical shear mechanism, a positive (negative) barotropic vorticity anomaly is produced to the north (south) of the convection center, resulting in a north–south asymmetry of PBL convergence and moistening, and thus promoting the northward propagation. The air–sea interaction mechanism is attributed to the near-quadrature relationship between the BSISO convection and sea surface temperature (SST) anomalies (Kemball-Cook and Wang 2001; Fu et al. 2003; Roxy and Tanimoto 2012). The observed warm SST anomalies to the north of the active BSISO convection (Wang et al. 2006) may exert a significant effect in the PBL moistening through enhancing the surface latent heat flux (Vecchi and Harrison 2002; Roxy and Tanimoto 2012; Wang et al. 2018) and PBL convergence (Wang et al. 2018). The above mechanisms of BSISO can be compared with the first school of thinking mentioned before, namely, the asymmetry of the PBL convergence/moistening and its destabilizing effect.

Recently, efforts have been made to understand the northward propagation of BSISO from the moisture mode paradigm through diagnosing the MSE (or moisture/moist entropy) budgets (Pillai and Sahai 2016; Adames et al. 2016; Jiang et al. 2018; Gao et al. 2019). It is agreed that the distinct ISO propagation between winter and summer

is mainly attributed to the seasonal variations in the mean moisture pattern (Adames et al. 2016; Jiang et al. 2018). The propagation direction of the BSISO is favored by the spatial asymmetry of the intraseasonal MSE tendency, in which the horizontal advection is the dominant contributor. In addition, a quantitative diagnosis shows that the contribution of intraseasonal SST anomalies can reach about 12–20% over active BSISO regions, through modifying surface fluxes (Gao et al. 2019). The difference in the interaction of moisture and circulation in presence of underlying SST anomalies may be the reason for the differential propagation (Pillai and Sahai 2016).

For the horizontal advection which is the dominant contributor of the intraseasonal moisture tendency that regulates the BSISO propagation, discrepancies exist in previous studies regarding the relative importance of its specific processes. In the unified moisture mode framework suggested by Jiang et al. (2018), the zonal advection of background moisture by the intraseasonal flow is almost the only term that controls the positive moisture tendency anomaly. However, Adames et al. (2016) shows that both the advection of mean moisture by the anomalous flow and advection of anomalous moisture by the mean zonal flow contribute significantly. While the zonal advection is particularly emphasized in the other studies, Gao et al. (2019) shows that the meridional advection dominated by the background flow could be more important over the Bay of Bangel and the western part of the western North Pacific.

In addition to the differential compositing scheme (Jiang et al. 2018), an important reason of the discrepancies regarding the relative importance of the specific processes is the sensitivity of the diagnosis results to the areas and phases selected. Regularly, the quantitative budget diagnosis is obtained by calculating the area mean of each term over a fixed domain at a fixed phase (e.g., Hsu and Li 2012; Adames et al. 2016; Wang et al. 2017; Jiang 2017; Jiang et al. 2018). However, for a propagating system that has a large spatial scale such as BSISO, distinct background states and anomalous circulation can be found not only over different areas, but also at different stages of its life cycle. For instance, Adames et al. (2016) found that the background flow advection could favor the propagation of the BSISO rainband, but such an effect varies with regions as the prevailing direction of the climatological monsoon flow varies spatially. A lack of consideration of such regional and phase sensitivities occurred in many previous studies.

The current work is aimed at providing a more comprehensive view of the moisture mode framework for the northward-propagating BSISO, by taking account of the regional and phase dependence. For this purpose, two areas of active BSISO with distinct background states, namely, the western North Pacific (WNP) and Bay of Bengal (BoB) are selected. Diagnoses of the column-integrated MSE budget are applied at the initiating and developing stages of the BSISO convection over each area. Similarity and contrast between these two areas at two different stages are investigated, so as to understand the principal processes that promote the northward propagation of the BSISO and how they vary within a BSISO life cycle.

The rest of the paper is organized as follow. Data and methods are introduced in Sect. 2. Section 3 describes the extraction of the BSISO signature and general features of its evolution. Section 4 analyzes the results of column-integrated MSE budget diagnoses. Summary and discussion are given in Sect. 5.

2 Data and methods

2.1 Data

The datasets used in this study include (i) daily-averaged Climate Forecast System Reanalysis (CFSR) low-resolution products provided by the National Centers for Environmental Prediction (NCEP) (Saha et al. 2010), (ii) observed daily outgoing longwave radiation (OLR) from the National Oceanic and Atmospheric Administration (NOAA) polar-orbiting satellites (Liebmann and Smith 1996), and (iii) daily sea surface heat fluxes from the Objectively Analyzed Air-Sea Fluxes (OAFlux) provided by the Woods Hole Oceanographic Institution (Yu and Weller 2007). The three-dimensional atmospheric reanalysis and model-output diabatic heating products of CFSR at 27 pressure-levels (from 1000 to 100 hPa) are adopted. The observed OLR is used to identify the BSISO convective perturbations. The sensible and latent heat fluxes in the OAFlux dataset are calculated with the bulk algorithm [given by Eqs. (3), (4) below]. The near-surface wind speed, together with the temperature and humidity information of the sea surface/near-surface air is also provided in the OAFlux dataset and adopted in the current study.

The CFSR and OLR datasets have the same latitude–longitude grid at a resolution of $2.5° \times 2.5°$, and the OAFlux is defined at 1° spatial resolution. To unify the spatial resolutions among datasets, the OAFlux data are transformed into the 2.5° grid with linear interpolation. The period of 1985–2009 for all the datasets is chosen in order to cover the time range of the OAFlux dataset. The boreal summer refers to the months June, July and August (JJA) in this study.

2.2 Column-integrated MSE budget diagnosis

The moist static energy M at a constant pressure level is defined as:

$$\mathrm{M} \equiv C_p T + L_e q + gz \tag{1}$$

where T is the air temperature, q is the specific humidity, z is the geopotential height, C_p is the specific heat capacity at constant pressure ($=1004\ \mathrm{J\ K^{-1}\ kg^{-1}}$), L_e is the latent heat of vaporization ($=2.5\times10^6\ \mathrm{J\ kg^{-1}}$), and g is the gravitational acceleration ($=9.8\ \mathrm{m{\cdot}s^{-2}}$). Following Neelin and Held (1987), the column-integrated MSE budget equation can be written as:

$$\begin{aligned}\langle \partial_t \mathrm{M}\rangle' &= -\langle \mathbf{V}\cdot\nabla_h \mathrm{M}\rangle' - \langle \omega \partial_p \mathrm{M}\rangle' \\ &+ \langle \mathrm{SWHR}\rangle' + \langle \mathrm{LWHR}\rangle' + \mathrm{SHF}\uparrow' + \mathrm{LHF}\uparrow'\end{aligned} \tag{2}$$

where $\mathbf{V}$ is the horizontal wind vector, ∇_h is the horizontal gradient operator, ω is the vertical pressure velocity, p is the pressure, SWHR and LWHR are the shortwave and longwave radiative heating rates, respectively, and SHF ↑ and LHF ↑ are the surface upward sensible and latent heat fluxes respectively. The angle brackets represent a mass-weighted vertical integration from the surface to 100 hPa level. In order to diagnose the MSE budget associated with the BSISO evolution, a 20–80-day band-pass filter (denoted by a prime) is applied to Eq. (2).

In this study, M and its horizontal and vertical advections [corresponds to the first and second terms in the right-hand side of Eq. (2), respectively] are calculated with the atmospheric reanalysis product of CFSR. SWHR and LWHR are derived from the CFSR model-output diabatic heating product, and SHF ↑ and LHF ↑ are derived from the OAFlux dataset. According to Yu and Weller (2007) and Yu et al. (2008), SHF ↑ and LHF ↑ in the OAFlux dataset are calculated with the bulk algorithm:

$$\mathrm{SHF}\uparrow = \rho C_p c_h U \Delta T \tag{3}$$

$$\mathrm{LHF}\uparrow = \rho L_e c_e U \Delta q \tag{4}$$

where ρ is the density of the air, c_h and c_e denote the turbulent exchange coefficients for sensible and latent heat fluxes respectively, U is the wind speed near the sea surface, ΔT and Δq are the temperature and specific humidity differences between the sea surface and near-surface air respectively. The terms $\rho C_p c_h$ and $\rho L_e c_e$ in Eqs. (3) and (4) can be calculated at every time step with the rest terms derived from the raw OAFlux dataset.

To identify the relative contributions of different time scales and their non-linear interaction effects in the intraseasonal MSE budget, a similar decomposition method used in Hsu and Li (2012) and Li et al. (2015) is applied:

$$X = \bar{X} + X' + X^* \tag{5}$$

where X represents any time-dependent variable, and is decomposed into a low-frequency background state component (> 80 day, denoted by an overbar), an intraseasonal component (20–80-day, denoted by a prime), and a high-frequency eddy component (< 20 day, denoted by an asterisk). Here both synoptic-scale perturbations (typically less than 10 days) and quasi-biweekly oscillations (typically 10–20-day) are included in the high-frequency eddy component.

Our calculation shows that associated with the BSISO evolution, the first-order approximation of the column-integrated MSE budget equation on the intraseasonal time-scale [Eq. (2)] can be written as:

$$\begin{aligned}\langle \partial_t \mathrm{M}\rangle' &\approx -\left\langle \bar{\mathbf{V}}\cdot\nabla_h \mathrm{M}'\right\rangle' - \left\langle \mathbf{V}'\cdot\nabla_h \bar{\mathrm{M}}\right\rangle' - \left\langle \omega' \partial_p \bar{\mathrm{M}}\right\rangle' \\ &+ \langle \mathrm{LWHR}\rangle' + \overline{\rho L_e c_e}\left(U'\overline{\Delta q} + \bar{U}\Delta q'\right)\end{aligned} \tag{6}$$

That is, the horizontal advections and latent heat flux are regulated by the interactions between the background states and intraseasonal perturbations. The advection of background MSE by the intraseasonal ascending/descending is dominated in the vertical direction. The effects of shortwave radiative heating and sensible heat flux are neglected due to their small magnitudes.

3 Extraction of the BSISO signature and general features of BSISO evolution

According to Fig. 1a which shows the tropical intraseasonal variabilities of convection during boreal summer, two active BSISO regions, the western North Pacific (WNP) and Bay of Bengal (BoB), are selected for diagnoses in this study. To extract local BSISO signals for WNP and BoB, an EOF (empirical orthogonal functions) analysis for 20–80-day OLR anomalies is applied to the boxes (WNP: 110°–135° E, 7.5°–22.5° N; BoB: 80°–100° E, 7.5°–17.5° N) with larger variabilities. These boxes (hereafter, "target regions") are selected partly because their longitude bands almost cover the entire BoB and WNP regions, and they also correspond well to the northward propagating routes of the BSISO, as will be seen below. The EOF results are generally insensitive to the small changes of boxes (figure not shown).

The two leading EOF modes over the WNP (Fig. 2a, b) and BoB (Fig. 2c, d) explained about two-thirds of the total variance in each target region for EOF analysis, respectively. The associated spatial structures are generally characterized by zonally-elongated OLR anomaly bands. The negative OLR anomaly in each EOF1 mode is centered near the northern flank of that in the corresponding EOF2 mode. The auto-correlations of the first principal components (PC1s) (black dashed lines in Fig. 3) are minimized when the lead/lag step is about 15 days, and the cross-correlations between each pair of PC1 and PC2 (blue solid lines in Fig. 3) are

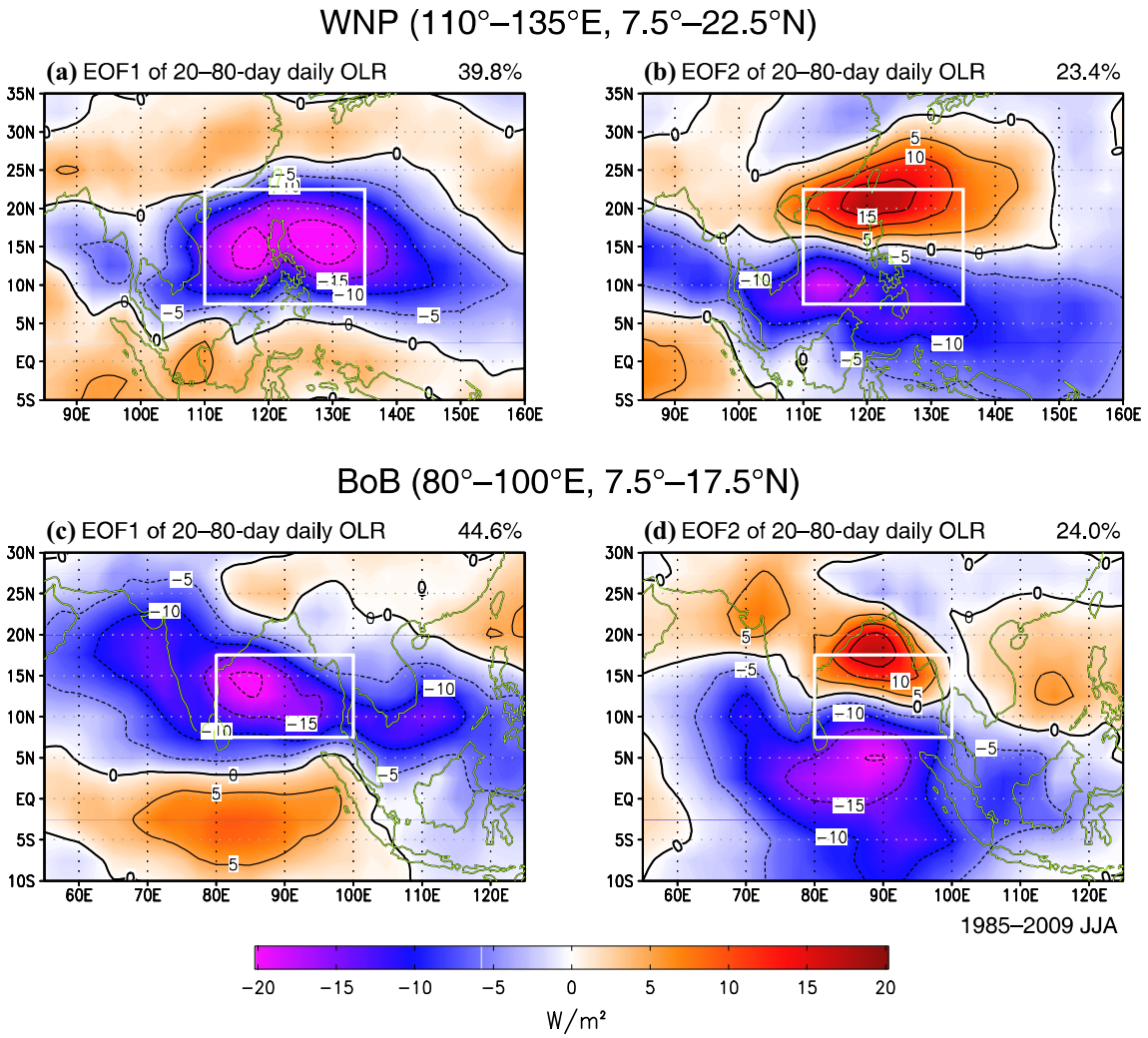

Fig. 2 Two leading EOF modes of 20–80-day band-pass filtered daily OLR anomalies in JJA for 1985–2009 over the WNP (**a**, **b**) and BoB (**c**, **d**) areas respectively, regressed upon the corresponding standardized principal components. The white boxes indicate the domains for EOF decomposition (WNP: 110°–135° E, 7.5°–22.5° N; BoB: 80°–100° E, 7.5°–17.5° N). Percentages of the variance explained by each mode are displayed on the top right corners

maximized (minimized) when PC2 leads (lags) PC1 by about 5–10 days. The above features suggest that the first two EOF modes over each target region capture a northward-propagating mode of convective anomalies with a principal period of 30–40 days.

The BSISO events over the WNP and BoB areas are identified with the PC1s of the EOF decompositions over the corresponding target regions. A total of 48 stronger events with the local maximums of PC1 exceeding one standard deviation are identified for each area, respectively. With these events, lead-lag composites are constructed for each area. Hereafter, day 0 refers to the time when PC1 reaches its local maximum, and negative (positive) days indicate the time before (after) day 0.

The composite temporal evolutions of the initiating and developing of an active BSISO convection over the WNP and BoB are shown in Figs. 4 and 5, respectively. The evolutions of the convectively suppressed phase share similar features but with opposite signs (not shown). For both the WNP and BoB areas, the BSISO convective perturbations originate from the equatorial Indian Ocean/western Pacific, then propagate northward and strengthen over the corresponding target regions of EOF analysis, and finally dissipate over the subtropical Asian continent. The northwest-southeast tilted rainband structure can be recognized according to the zonally-elongated OLR anomaly bands. Such a tilting is particularly obvious over the BoB area.

The anomalous circulation associated with the northward-propagating BSISO is governed by the modified Gill-type

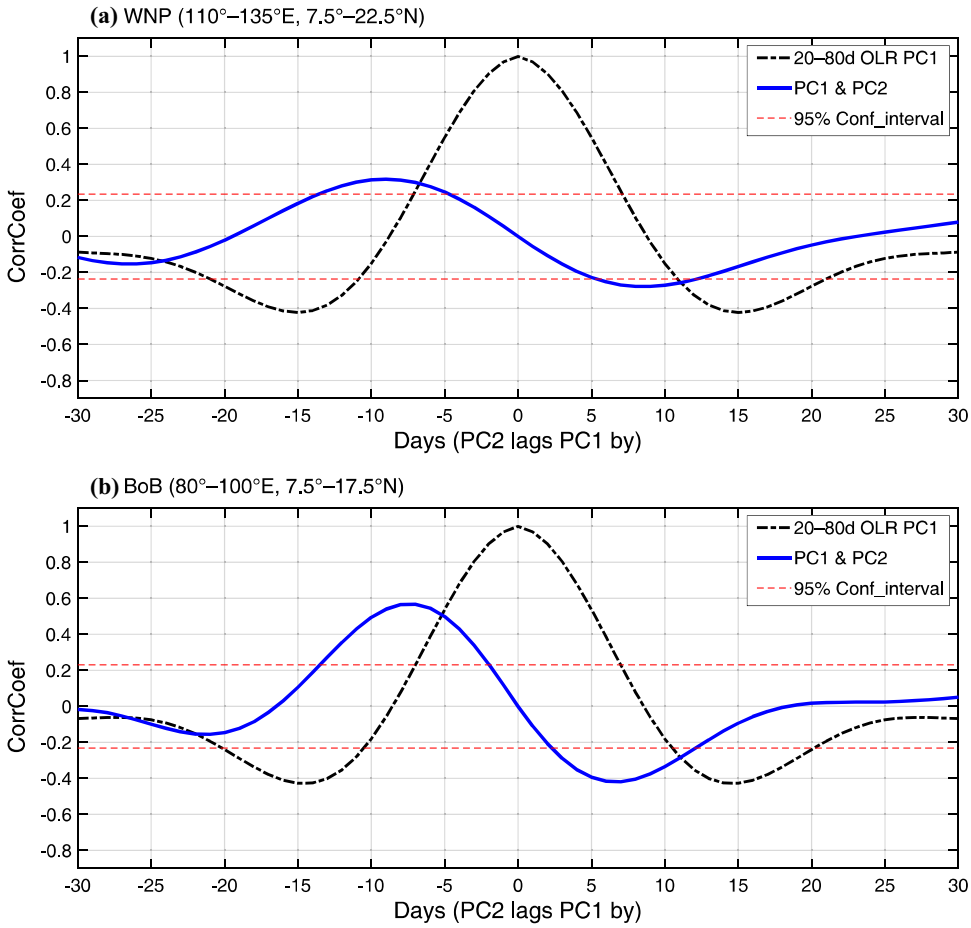

Fig. 3 Autocorrelations of the first principal components (PC1s, black dashed lines) of the EOF decompositions shown in Fig. 2, and the cross-correlations between each pair of PC1 and PC2 (blue solid line), for **a** WNP and **b** BoB areas respectively. The ordinates are the correlation coefficients where the red long-dashed lines are bounds of the 95% confidence interval (Student's *t* test). The abscissas are the lead/lag time in days with positive (negative) values indicating that PC1 or PC2 lags (leads) PC1

response and off-equatorial Rossby wave response to convective heating, both under the vertical easterly shear of background summer monsoon (Wang and Xie 1996; Xie and Wang 1996; Wang et al. 2003; Jiang and Li 2005). In this case, the anomalous low-level cyclonic (anti-cyclonic) circulation has a slight northward shift relative to the enhanced (suppressed) convection center. Observed strong low-level easterly anomalies thus appear to the north and along the northern flanks of the convective area, and strong westerly anomalies are located over the southern portion of an off-equatorial convection.

Distinct spatial and temporal phase relationships among several key variables can be identified in Figs. 4 and 5, as well as from the time-latitude sections (Fig. 6) and the target region averaged time series (Fig. 7). An active BSISO convection is accompanied with a positive intraseasonal column-integrated MSE perturbation ($\langle M \rangle'$), while the tendency of the latter ($\langle \partial_t M \rangle'$) is generally in-phase with the intraseasonal SST anomaly. A near-quadrature phase relationship exists between BSISO convection/$\langle M \rangle'$ and SST anomaly/$\langle \partial_t M \rangle'$. That is, positive $\langle \partial_t M \rangle'$ and warm SST anomalies appear before/to the north of the BSISO convection with a phase shift by roughly 90°.

The time-latitude section (Fig. 6) clarified a marked north–south asymmetry of $\langle \partial_t M \rangle'$ about the BSISO convection center, with positive (negative) anomalies to the north (south). According to the moisture mode theory, such an asymmetry of MSE tendency promotes the northward propagation of the BSISO convection. Figure 6 also reveals that for the northward propagation of an active BSISO convection, the north–south asymmetry is mainly driven by the positive $\langle \partial_t M \rangle'$ to the north. The key issue of the current work is to diagnose the causes of the observed north–south asymmetry of $\langle \partial_t M \rangle'$, which would be examined in the following section.

4 Intraseasonal column-integrated MSE budget diagnoses

4.1 Phase selection and general characteristics

The residuals of the diagnosed results of intraseasonal column-integrated MSE budget in the current study are acceptable, which is verified in Fig. 7. For the target region-averaged temporal evolutions, both the diagnosed results

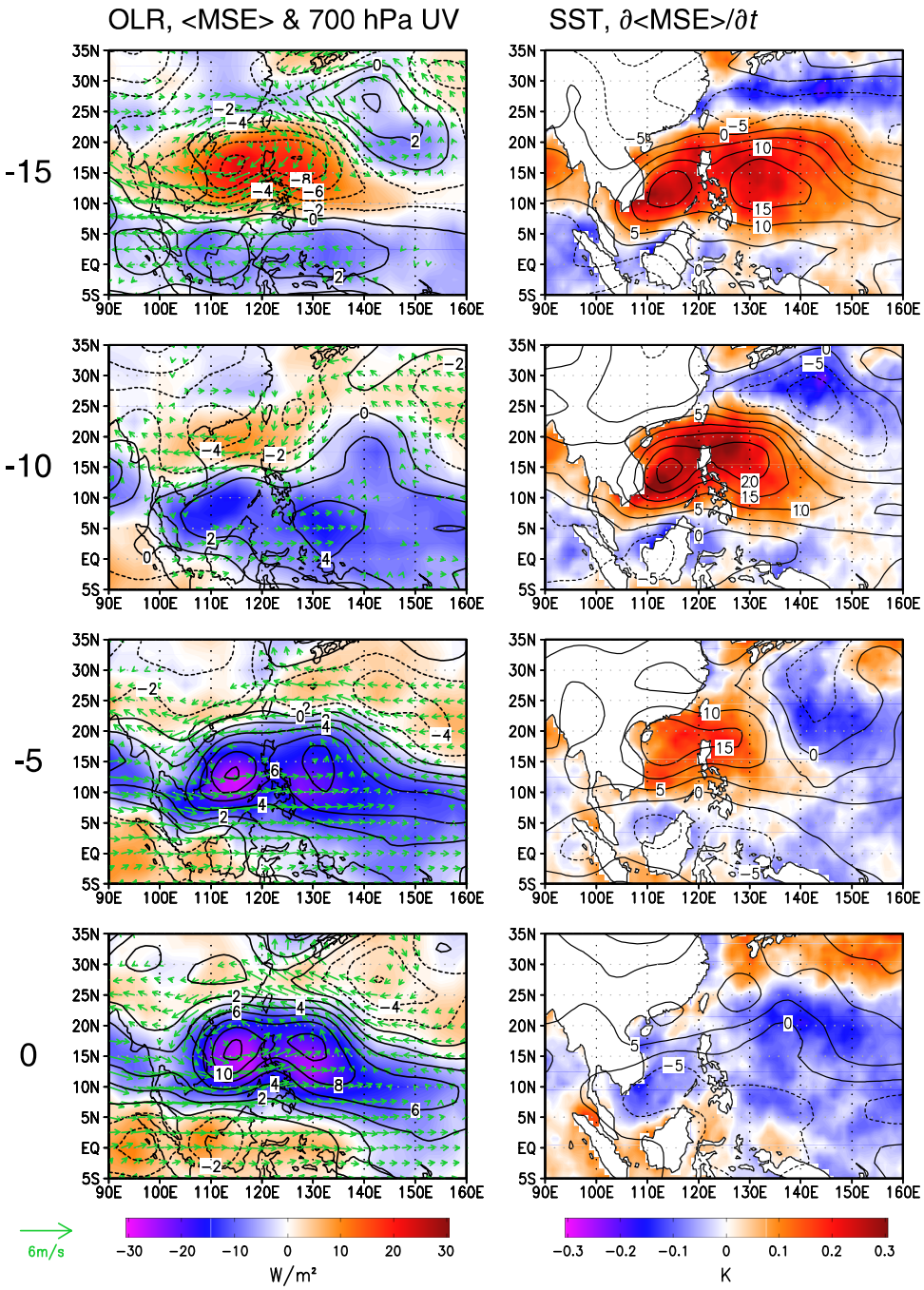

Fig. 4 Left panel: composite intraseasonal anomalies of daily OLR (shaded), column-integrated MSE (contour, interval: 2×10^6 J/m^2), and 700 hPa horizontal wind flows (vectors) centered at lead/lag days − 15, − 10, − 5 and 0, in terms of the BSISO events identified with PC1 over the WNP target region. Right panel: same as the left panel, but for SST (shaded) and column-integrated MSE tendency (contour, interval: 5 W/m^2)

without [i.e., sum of the right-hand side of Eq. (2), magenta lines] and with first-order approximation given by Eq. (6) (green dashed lines) match well with $\langle\partial_t \mathrm{M}\rangle'$ itself (black dotted lines), particularly over the WNP area. Albeit detectable deviations exit over the BoB area on both the magnitudes and phases, the diagnosed results captured the general features. Residuals may come from the finite-difference calculation, the inconsistency between datasets, and also the neglected terms for the first-order approximation.

In order to taking account of the phase dependence, two stages of a BSISO convection are selected over each area for comparison. One is the initiating stage centered at day-15 (indicated by green triangles in Fig. 6), during which the convective signal emerges over the equatorial area, accompanied with large MSE tendency anomalies to the north. Another is the developing stage centered at day-8 (indicated by yellow triangles in Fig. 6). At the developing stage, the northward-propagating convection is enhanced, and pronounced north–south asymmetry of the $\langle\partial_t \mathrm{M}\rangle'$ still exists. The mature phase (day 0) when the convection is most enhanced is not selected, since the convection is decaying

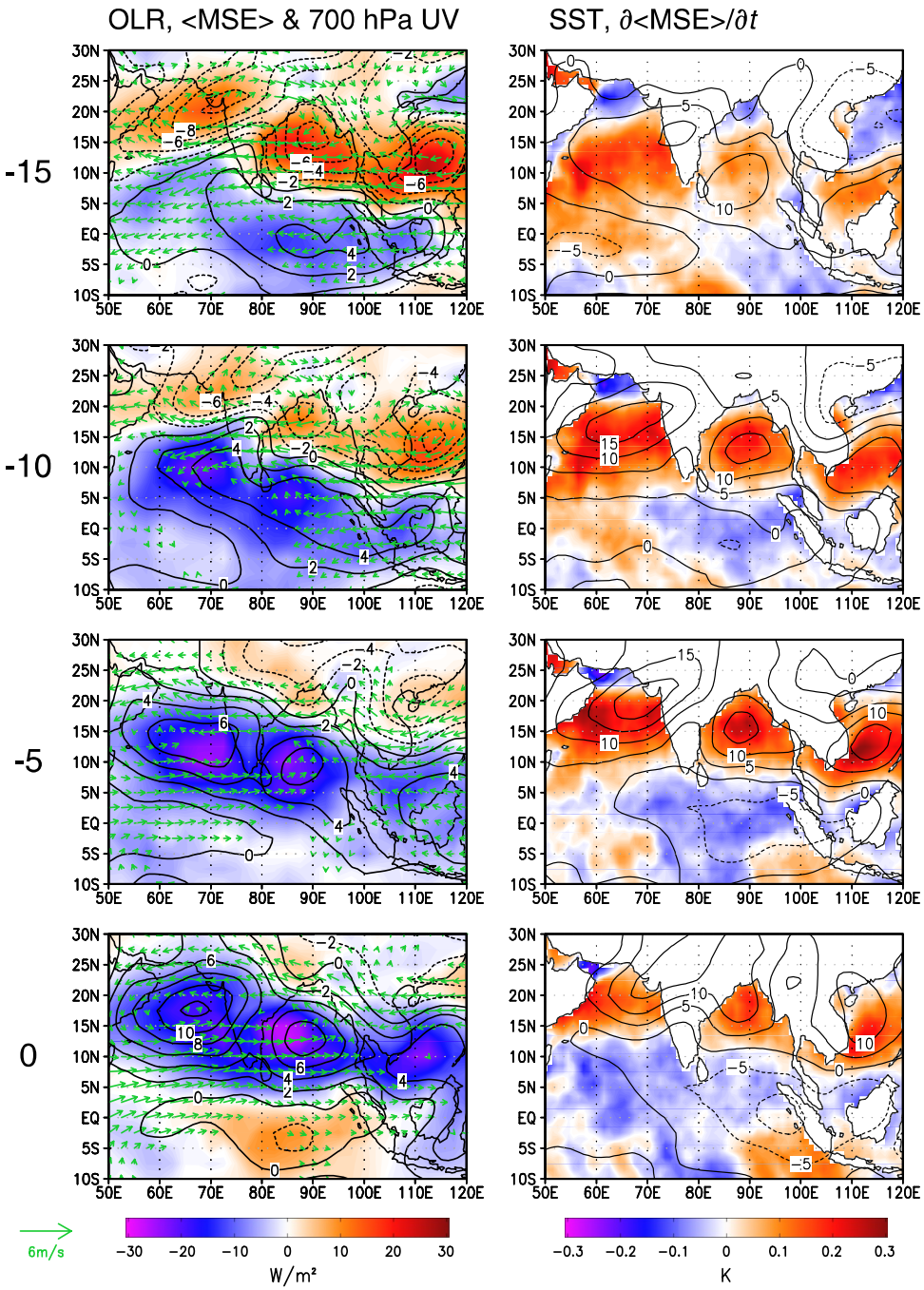

Fig. 5 Same as in Fig. 4, but the composites are in terms of the BSISO events identified with PC1 over the BoB target region

rapidly after this stage, as the positive $\langle \partial_t \mathrm{M} \rangle'$ to the north is rather weak.

In order to understand the causes of the observed north–south asymmetry of $\langle \partial_t \mathrm{M} \rangle'$ that promotes the northward propagation of BSISO, we calculated the contribution of each term averaged over an area between the convection center and the descending center to the north, along the longitude band of each target region. The grids of the ascending and descending centers are excluded, since the processes there mainly contribute to the enhancing or decaying of the BSISO, but not the propagation. The $\langle \partial_t \mathrm{M} \rangle'$ to the south of the convection center is rather weak and is not in consideration. A 5-day average centered at day-15 and -8 gives the results for initiating and developing stages, respectively. For instance, as shown in Fig. 10, the area for diagnosis at this moment ranges from 5° to 12.5° N (indicated by white dashed lines) along the WNP longitude band, since the convection and descending centers are located at around 2.5° N and 15° N, respectively, and the datasets have a spatial resolution of 2.5°. The final results for the initiating stage are obtained from the

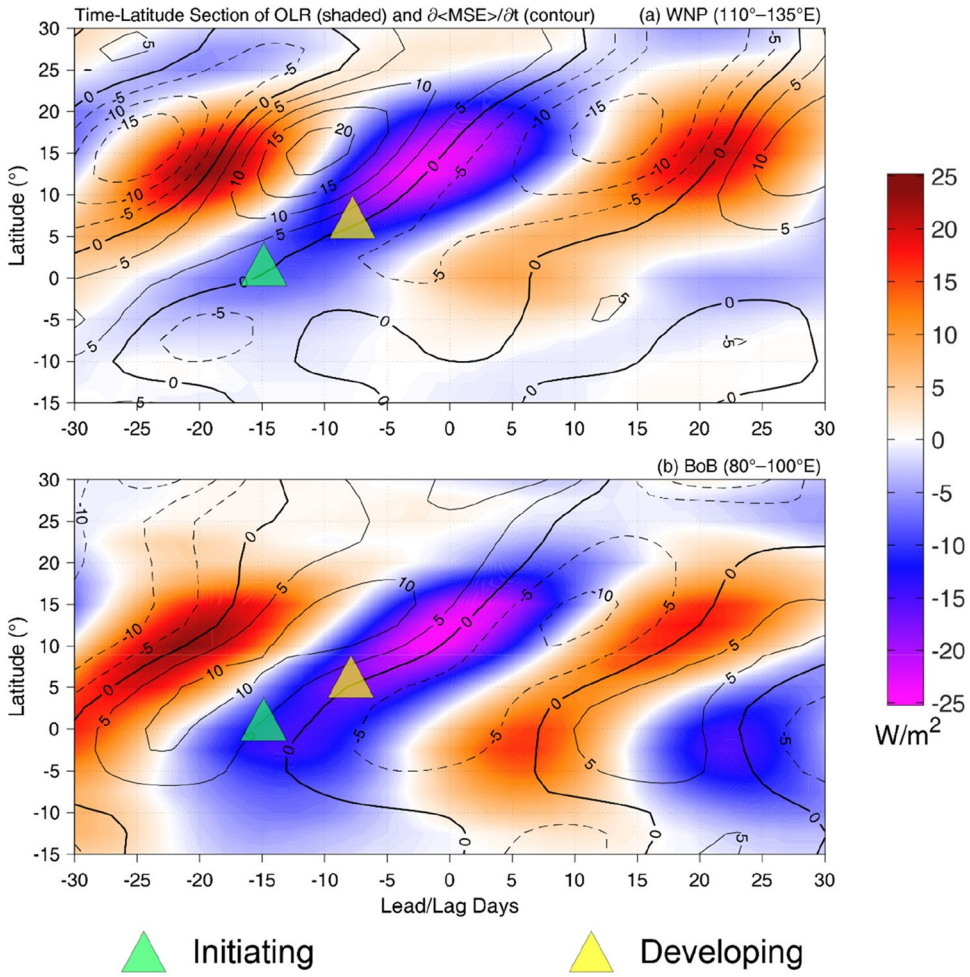

Fig. 6 Time-latitude section of composite intraseasonal OLR (shaded) and column-integrated MSE tendency anomalies (contour, interval: 5 W/m^2) along the (**a**) WNP and (**b**) BoB target region longitudes. Green and yellow triangles indicate the points of the initiating and developing stages of an active BSISO convection

average of day-17 to day-13, and the diagnosis area adjusts to the propagation of the convection and descending centers at every lead/lag day.

The diagnosed results for the north–south asymmetry of $\langle \partial_t \mathrm{M} \rangle'$ at initiating and developing stages over the WNP and BoB areas are given in Fig. 8. Figure 9 shows the area differences of Fig. 8. As revealed in the figures, the asymmetry of $\langle \partial_t \mathrm{M} \rangle'$ is mainly driven by the advection processes, while the external sources of $\langle \mathrm{M} \rangle'$, namely, the longwave radiative heating ($\langle \mathrm{LWHR} \rangle'$) and surface upward latent heat flux (LHF $\uparrow'$) appear to inhibit it. The relative importance of each term varies with regions and phases. The detailed characteristics and causes of each term will be discussed below.

4.2 Intraseasonal vertical motion effects

The vertical advection as well as the longwave radiative heating ($\langle \mathrm{LWHR} \rangle'$) processes are attributed to the intraseasonal vertical motion effects. This is because the former is dominated by the vertical advection of background MSE by the intraseasonal vertical motion ($-\left\langle \omega' \partial_p \bar{\mathrm{M}} \right\rangle$), and the latter is largely regulated by cloud covers related to ω'. There is an obvious phase dependence of the intraseasonal vertical motion effects as shown in Fig. 8, that is, they are particularly important at the initiating stage but negligible at the developing stage. The regional dependence, on the other hand, is minor (Fig. 9), which makes the analysis convenient as the regional comparison can be ignored.

The vertical-latitude cross sections of several key variables related to the intraseasonal vertical motion effects centered at the initiating stage are shown in Fig. 10, which is averaged along the longitude of the WNP target region. Similar features can be found over the BoB area (not shown). The BSISO convection near the equator at the initiating stage can be clearly identified in the vertical sections of M' (shading in Fig. 10a) and ω' (contours in Fig. 10b). Meanwhile, a much stronger intraseasonal subsidence anomaly is found to the north than to the south.

The much stronger subsidence anomaly to the north than the south of the convection near the equator is mainly caused by the equatorial asymmetry of the summer mean state. During boreal summer, the intertropical convergence zone shifts northward, so that more active convections appear to the north of the equator while it is regulated by descending

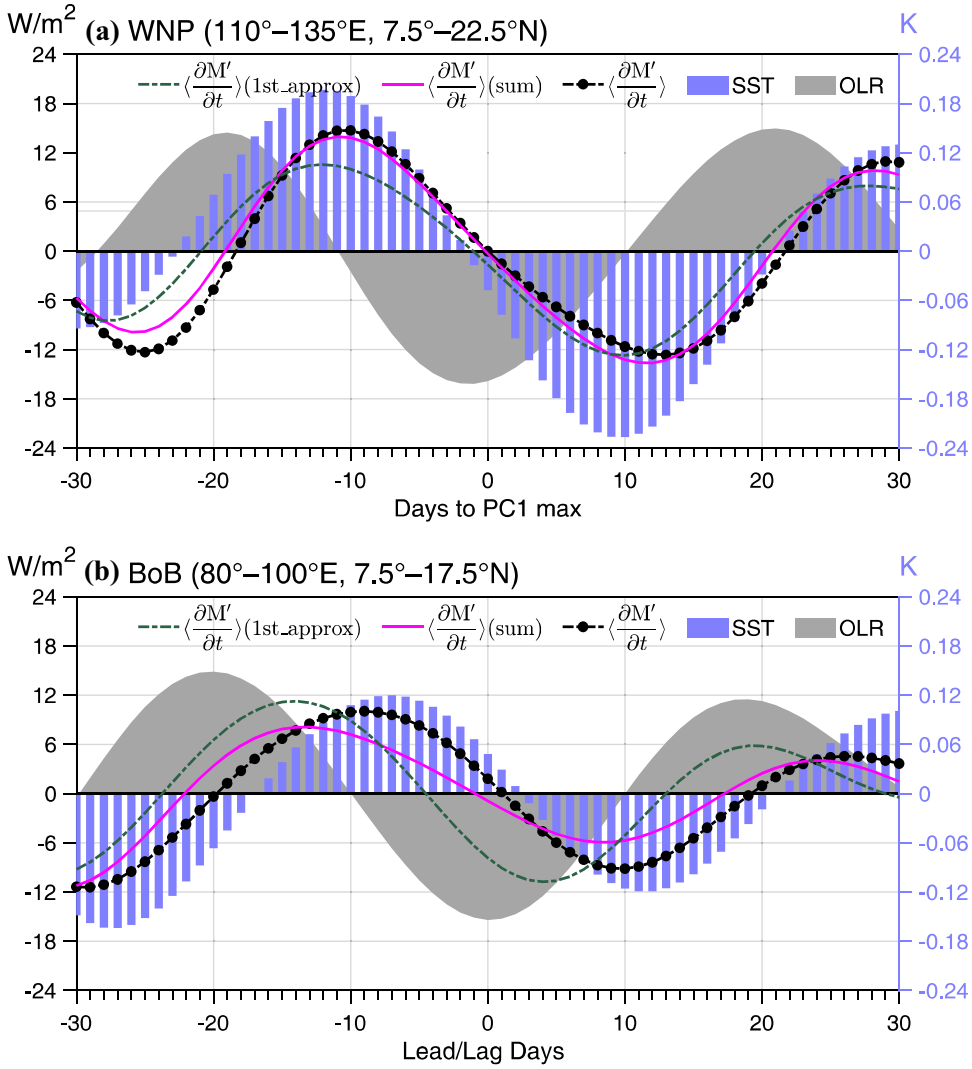

Fig. 7 Temporal evolutions of the composite intraseasonal anomalies spatially averaged in the **a** WNP and **b** BoB target regions, for column-integrated MSE tendency (black dotted lines), its diagnosed result by Eq. (2) (magenta lines), and the diagnosed result of the first-order approximation by Eq. (6) (green dashed lines). For comparison, the corresponding composite SST (blue bars) and OLR (grey areas) anomalies are displayed

motions to the south. In this case, a subsidence perturbation resulted from the BSISO meridional-vertical overturning circulation may exert a significant effect over the northern tropics by inhibiting the prevailing convections. The weakened convection leads to a reduced diabatic heating, which further enhances the anomalous subsidence and forms a positive feedback. However, an additional subsidence does not lead to an anomalous diabatic heating over the southern tropics where the background state is dominated by descending motions.

In addition to the equatorial asymmetry of the summer mean state, another two factors are possibly responsible for the stronger subsidence anomaly to the north. One is the upper-tropospheric stratiform heating at the rear of the BSISO convection as revealed by the contours of ω' in Fig. 10b, which could be related to the upper-level stratiform cloud detected at the rear of the winter MJO convection (Lin et al. 2004; Wang et al. 2017). Another is the ascending motion over the subtropical Asian continent that comes from the decaying BSISO convection of the previous round. These additional ascending motions appear to enhance the subsidence to the north of the BSISO convection near the equator. The stratiform heating also weakens the upper-level subsidence to the south of the convection center, which amplifies the north–south asymmetry of the anomalous vertical motion. At the developing stage (Fig. 11), the BSISO convection has moved away from the equator, and both the additional ascending motions vanished, so that the meridional-vertical overturning circulation becomes more symmetric about the convection center.

The much stronger subsidence anomaly to the north of the convection near the equator makes an asymmetric contribution of the intraseasonal vertical motion effects to the $\langle \partial_t \mathrm{M} \rangle'$. As the summer mean MSE is minimized in the middle and lower troposphere (could be identified from the level of zero $-\langle \omega' \partial_p \bar{\mathrm{M}} \rangle'$ shown in Figs. 10b and 11b), a deep subsidence results in a positive vertically integrated background MSE advection. On the other hand, the subsidence anomaly leads

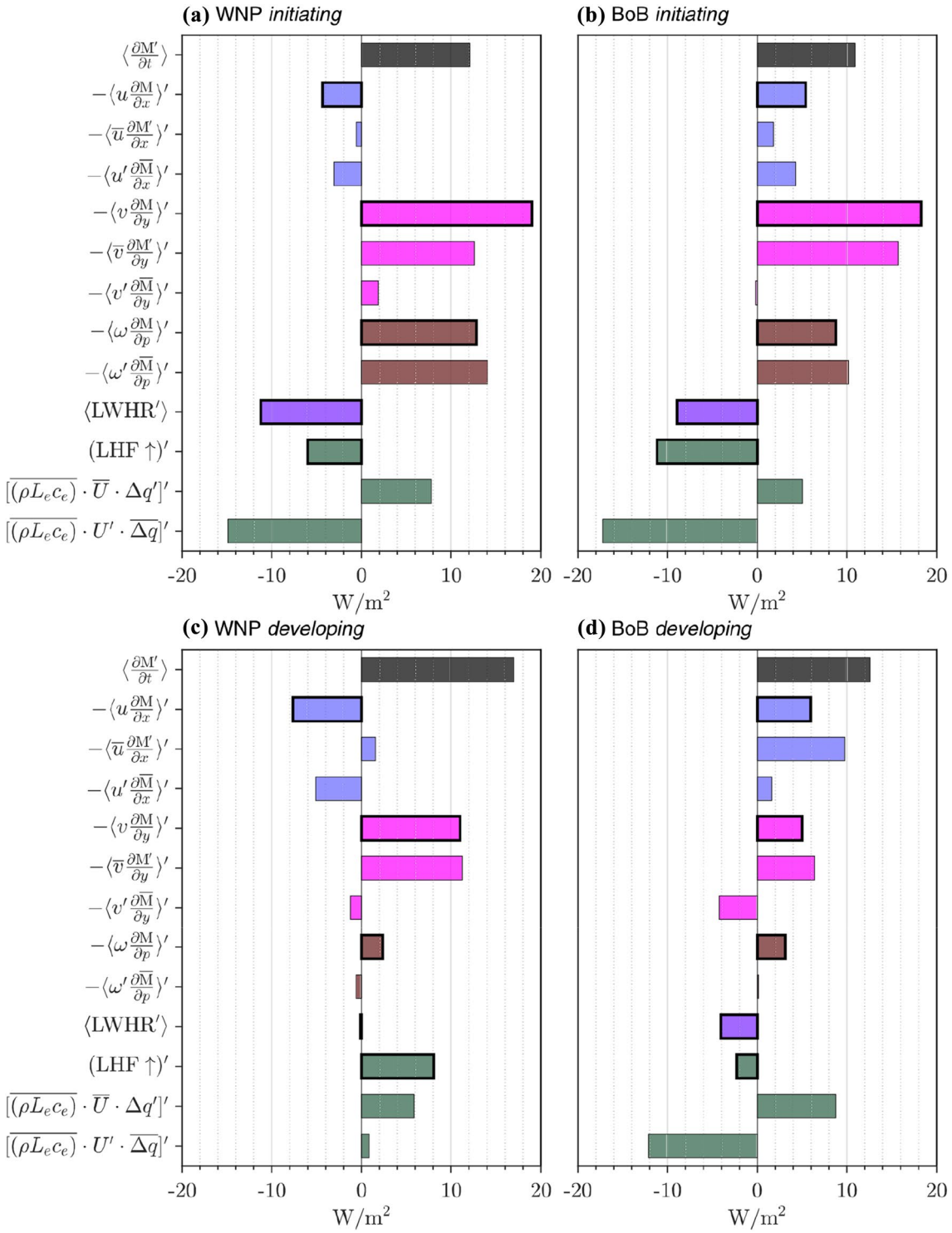

Fig. 8 Composite intraseasonal anomalies of column-integrated MSE tendency and its principal contributors at initiating (upper panels) and developing (lower panels) stages for WNP (left panels) and BoB (right panels), averaged over the area between the ascending and descending centers along the longitude of each target region

to less cloud cover and more outgoing longwave radiation, so that the $\langle \mathrm{LWHR} \rangle'$ term becomes negative. Therefore, with a much stronger subsidence anomaly to the north of the convection at the initiating stage, the intraseasonal vertical motion contributes positively to the observed north–south asymmetry of $\langle \partial_t \mathrm{M} \rangle'$ through vertical MSE advection, but it

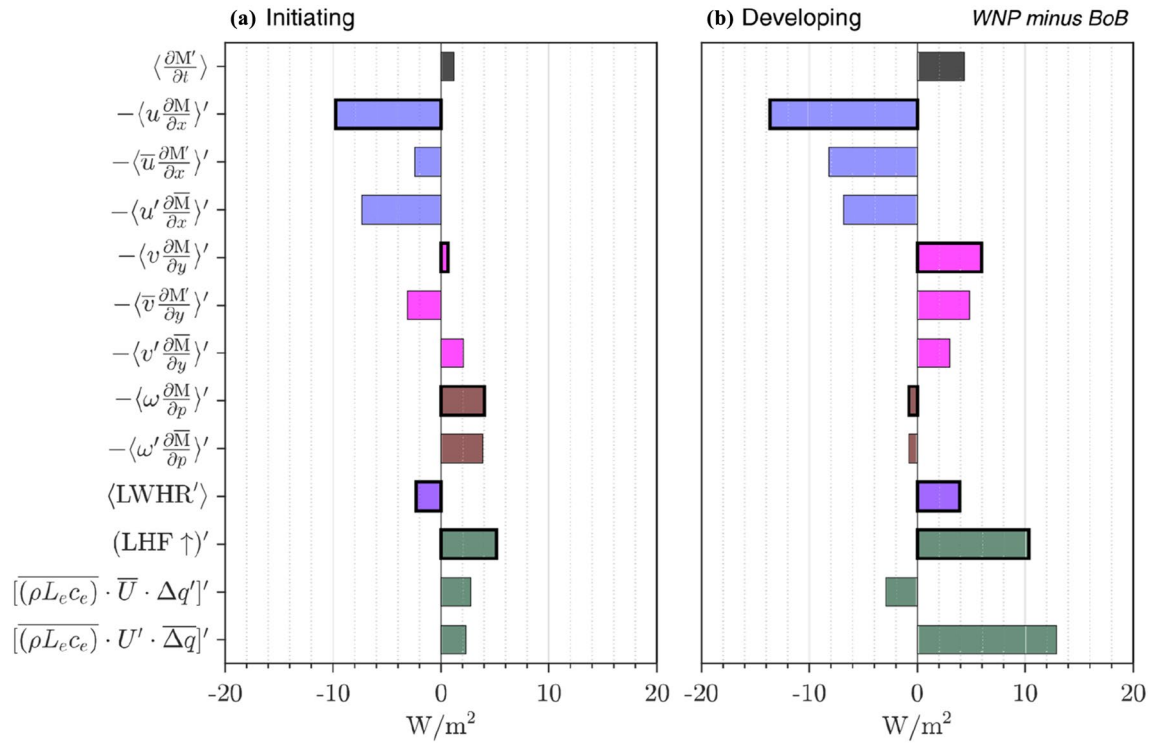

Fig. 9 Same as in Fig. 8, but for the difference between WNP and BoB at **a** initiating and **b** developing stages

is partially offsets by the reduced longwave radiative heating. As the meridional-vertical overturning circulation becomes more symmetric about the BSISO convection center at the developing stage, the intraseasonal vertical motion effects are negligible.

4.3 Horizontal advections

The horizontal advections exhibit more complicated characteristics than the vertical motions. Both zonal and meridional components, as well as the advections by background and intraseasonal flows are retained in the first-order approximation. Besides, there is pronounced regional and phase dependence. For simplicity, the horizontal advection processes are analyzed at 700 hPa, since the intraseasonal perturbations of $\langle M \rangle'$ and $\langle \partial_t M \rangle'$ are maximized around this level as shown in the vertical sections (Figs. 10a and 11a).

As the advections of background MSE and advections by background flow are both important, Fig. 12 provides the information of climatological horizontal distributions of 700 hPa MSE and wind fields. The background low-level MSE is maximized over the Asian land region, as it is largely regulated by the thermal effect (contours represent the ratio of enthalpy to MSE). It is also higher over the surrounding oceans/Maritime Continent than over the oceans far away from the land. The background low-level circulation is depicted by the Asian summer monsoon, with strong westerly over the BoB and southerly over the WNP. It is worth pointing out that over the most part of the BoB, there also exists southerly component with almost the same magnitude of that over the WNP. For further analysis, a combination of background (intraseasonal) MSE and intraseasonal (background) circulation is given in Fig. 13.

The background flow governs the horizontal advection processes in the BSISO MSE budgets. As exhibited in Fig. 13e, f, with maximized MSE anomalies over the convective area, the advection by the southerly component of background flow ($-\langle \bar{v}\partial_y M' \rangle'$) contributes mostly to the positive $\langle \partial_t M \rangle'$ to the north (denoted by thick contours). In addition, the zonal advection ($-\langle \bar{u}\partial_x M' \rangle'$) is particularly important over the BoB at the developing stage. Figure 13f reveals that the BSISO rainband (positive M') has a marked northwest-southeast tilted structure, so that strong background westerly transports higher MSE anomalies over its northwest downstream. However, due to weak background westerly or less titled rainband, large $-\langle \bar{u}\partial_x M' \rangle'$ does not exist in the other cases.

The advections of background MSE by the intraseasonal horizontal circulation exert relatively smaller effects. As the Asian land with higher background MSE locates to the west of WNP, easterly anomalies to the north of the convection results in negative $-\langle u'\partial_x \bar{M} \rangle'$ (Fig. 13b). In contrast, the BoB is surrounded by the Indian Subcontinent

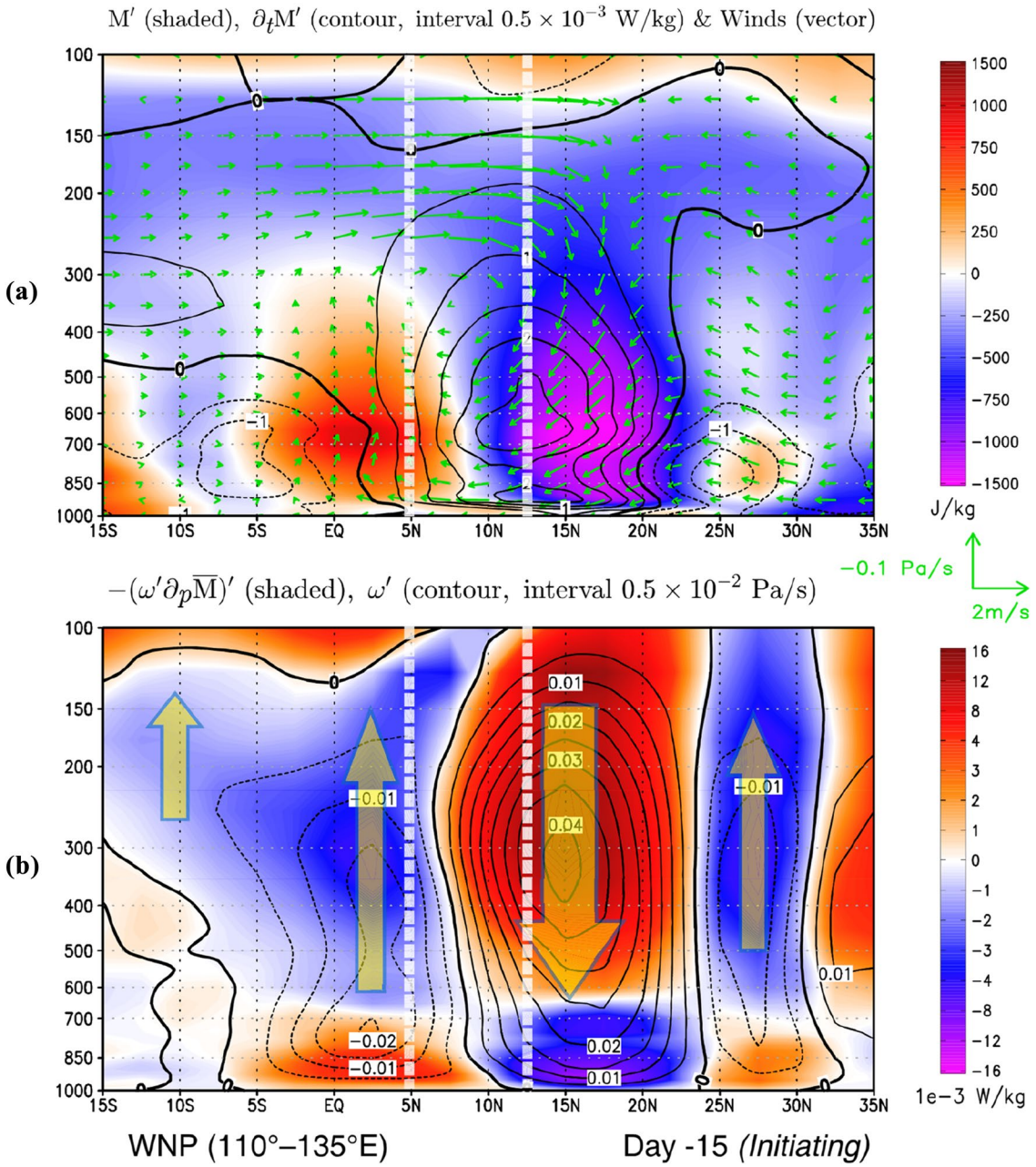

Fig. 10 Vertical-latitude cross sections of composite intraseasonal anomalies along the longtiduted of the WNP target region (110°–135° E) at lead/lag day − 15, for **a** MSE (shaded), MSE tendency (contour, inteval: 0.5×10^{-3} W/kg), and circulation (vectors); **b** vertical advection of background MSE by intraseasonal flow (shaded), and vertical pressure velocity (contour, interval 0.5×10^{-2} Pa/s). White dashed lines indicate the southern and northern boundaries in calculating the regional averaged diagnosed results. Arrows in **b** indicate the crucial intraseasonal vertical motions that contribute to the north–south asymmetry of $\langle\partial_t \mathrm{M}\rangle'$

and Indochina Peninsula where zonal gradient of $\bar{\mathrm{M}}$ is weak (Fig. 13c), so that the advection by anomalous zonal flow generally has little impact. The weak but positive $-\langle u'\partial_x\bar{\mathrm{M}}\rangle'$ detected at its initiating stage is due to the relatively higher $\bar{\mathrm{M}}$ over the Maritime Continent. The $-\langle v'\partial_y\bar{\mathrm{M}}\rangle'$ terms are always negligible, as v' is weak along the northern flanks of the convection.

The pronounced regional difference of the horizontal advection processes is generally characterized by a more important role of zonal advection over the BoB than over the WNP. As mentioned before, the differential advections by anomalous zonal flow due to distinct land-sea distributions lead to such a regional difference (Fig. 13a–c). The much stronger background westerly over the BoB becomes a more important factor and amplifies such a difference at

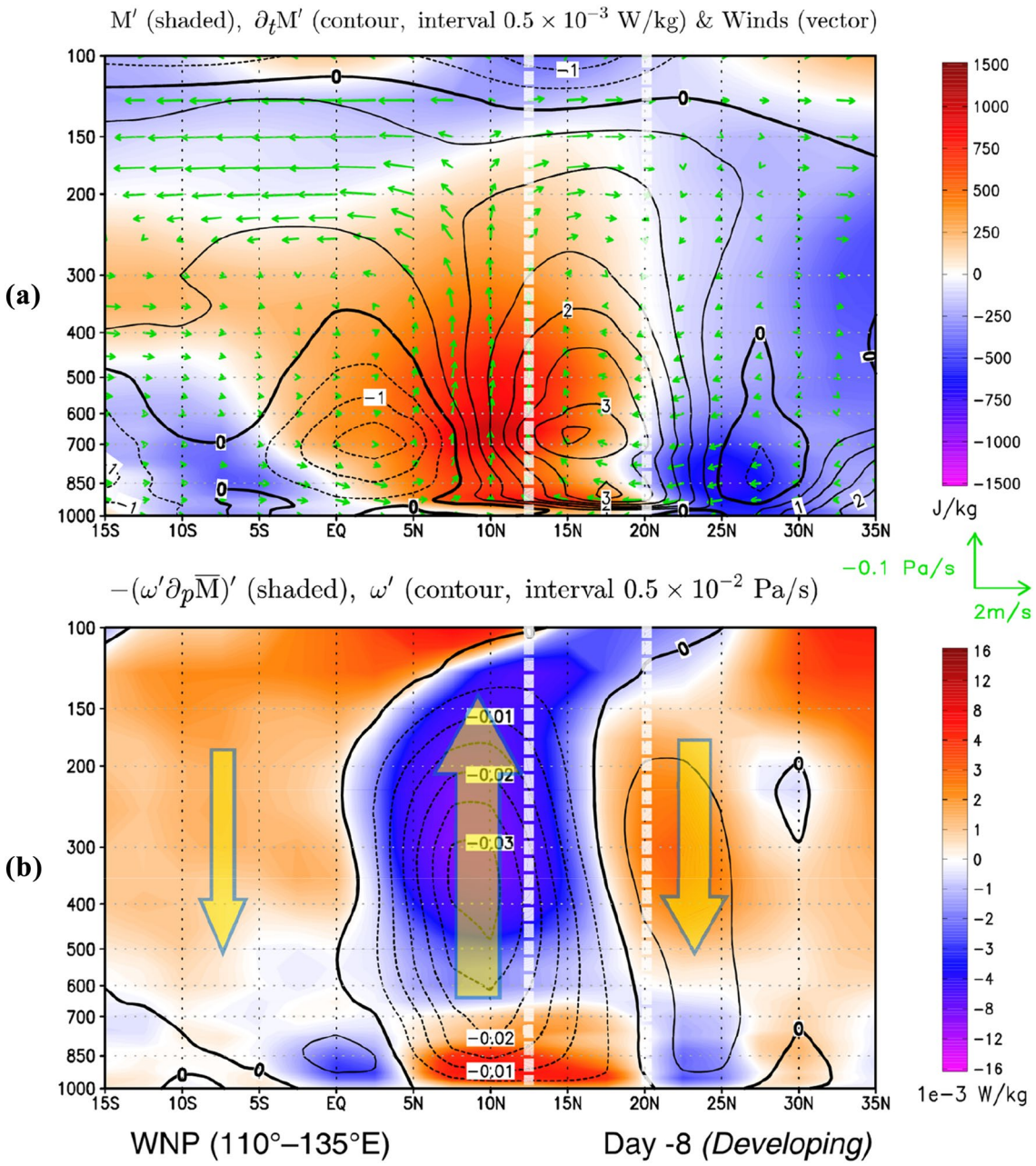

Fig. 11 Same as in Fig. 10, but at lead/lag day − 8

the developing stage (Fig. 13d–f). In addition, the prevailing southerly over the off-equatorial WNP results in a larger contribution of meridional advection at this stage, in comparison with that over the BoB.

The diagnoses of the horizontal advection processes reveal that in contrast to the winter MJO that the advection of background MSE by intraseasonal flow plays a leading role (e.g., Kim et al. 2014; Wang et al. 2017), the advection of the intraseasonal MSE by background flow is dominant in the BSISO. This is mainly due to the southwesterly/southerly background monsoon flow, along with the northwest-southeast tilted structure of BSISO rainband. The distinct land-sea distributions and prevailing wind directions result in pronounced regional and phase dependence.

4.4 Surface heat fluxes

Both surface sensible and latent heat fluxes are external sources of the column-integrated MSE and contribute to its tendency. The sensible heat flux has a relatively weak intraseasonal variability and is neglected in the first-order approximation. Besides, the sensible and latent heat fluxes

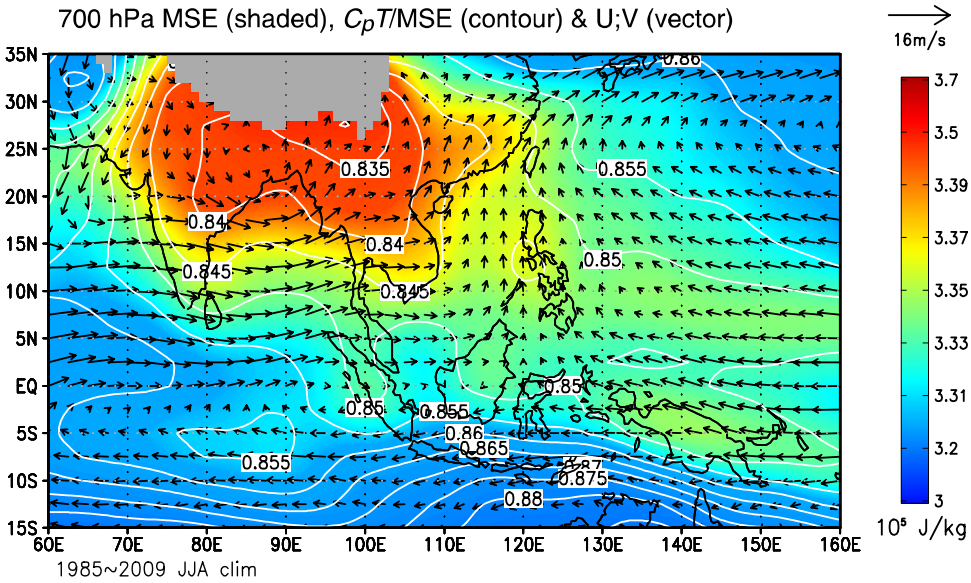

Fig. 12 Climatological horizontal distribution of 700 hPa MSE (shaded) during boreal summer (JJA) for 1985–2009. The contours indicate the ratio of enthalpy to MSE, and the vectors indicate horizontal wind fields

as well as their principal components share many common features associated with the BSISO evolution. Therefore, only the effect of the intraseasonal surface upward latent heat flux (LHF $\uparrow'$) is discussed.

It is found in Fig. 8 that the intraseasonal near-surface wind speed related component ($\overline{\rho L_e c_e} \cdot U' \overline{\Delta q}$) of the LHF $\uparrow'$ is the largest term that reduces the positive $\langle \partial_t \mathrm{M} \rangle'$ to the north of the convection in most cases, while it is partially compensated by the intraseasonal sea-air specific humidity difference related component ($\overline{\rho L_e c_e} \cdot \bar{U} \Delta q'$), resulting in a negative LHF $\uparrow'$. The only exception takes place over the WNP area at the developing stage.

The negative $\overline{\rho L_e c_e} \cdot U' \overline{\Delta q}$ term with large amplitude is caused by the configuration of surface background southwesterly and intraseasonal easterly to the north of the convection (e.g., Fig. 14a, b). The near-opposite direction between the background and anomalous winds significantly reduces the near-surface wind speed, thus suppressing the evaporation to the north of the convection.

The suppressed surface evaporation together with the enhanced insolation over the BSISO subsidence area generate an intraseasonal warm SST anomaly (Kemball-Cook and Wang 2001; Roxy and Tanimoto 2012; Wang et al. 2018). As the low-level cyclonic anomaly has a northward shift relative to the convection center in the existence of the background vertical shear (Jiang et al. 2004; Drbohlav and Wang 2005; Tsou et al. 2005), the easterly anomaly and associated suppressed evaporation largely coincides with the enhanced insolation (Wang et al. 2018). Due to the large heat capacity of the ocean mixed layer, the forced warm SST anomaly lags (leads) the subsidence (convection) by roughly 90-degree, and coincides with positive $\langle \partial_t \mathrm{M} \rangle'$ (Figs. 4, 5, 7, 14). In general, the sea-air specific humidity difference is mainly regulated by the SST. A positive $\overline{\rho L_e c_e} \cdot \bar{U} \Delta q'$ term thus appears to the north of the convection where SST anomaly is warm, which partially compensates the impact of reduced near-surface wind speed.

Although LHF $\uparrow'$ inhibits the observed north–south asymmetry of $\langle \partial_t \mathrm{M} \rangle'$ in most cases, an exception takes place over the WNP area at the developing stage. The positive LHF $\uparrow'$ to the north of the convection (Figs. 8, 15a) over the WNP has also been reported in Wang et al. (2018). As the $\overline{\rho L_e c_e} \cdot \bar{U} \Delta q'$ term has a comparable magnitude with those in other cases (Figs. 8, 15c, d), the direct cause of this exception is the nearly vanished impact of the $\overline{\rho L_e c_e} \cdot U' \overline{\Delta q}$ term (Figs. 8c, 15e). This is because the surface background flow over the off-equatorial WNP turns to be southerly dominant, so that the easterly anomaly no longer efficiently reduces the near-surface wind speed at this moment (Fig. 14c, d). In addition, the warm SST anomaly is a forced result of insolation and latent heat flux, whose intraseasonal variabilities are comparable associated the BSISO evolution (Roxy and Tanimoto 2012; Wang et al. 2018). It is thus reasonable that the feedback of the warm SST anomaly could reverse the negative sign of LHF $\uparrow'$, as long as the near-surface wind speed anomaly has a minor impact.

5 Summary and discussion

5.1 Summary

The intraseasonal column-integrated moist static energy ($\langle \mathrm{M} \rangle'$) budgets associated with the northward-propagating BSISO are diagnosed in this study, so as to improve the current understandings of the BSISO northward propagating mechanisms under the moisture mode framework.

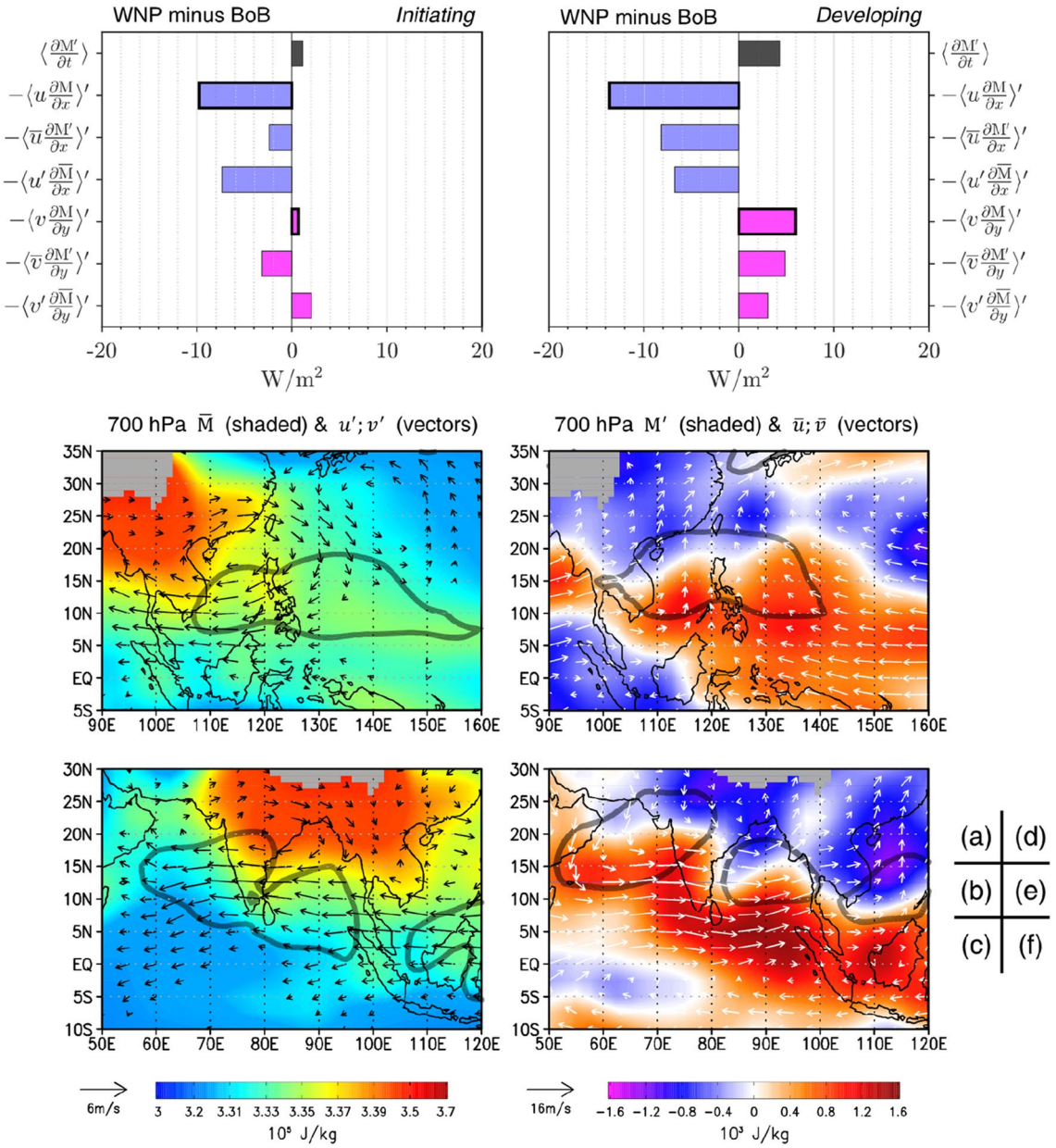

Fig. 13 **a**, **d** Same as in Fig. 9a, b, but only those terms related to horizontal advection processes are listed. **b**, **c** 700 hPa climatological MSE (shaded) and intraseasonal circulation (vectors) at the initiating stage for WNP and BoB areas, respectively. **e**, **f** 700 hPa intraseasonal MSE anomalies (shaded) and climatological circulation (vectors) at the developing stage for WNP and BoB areas, respectively. Thick contours surround the areas where $\partial_t\langle \mathrm{M}\rangle$ are larger [$\partial_t\langle \mathrm{M}\rangle \geq 10\mathrm{W/m^2}$ for (**b**), (**e**), (**f**), but $\partial_t\langle \mathrm{M}\rangle \geq 7\mathrm{W/m^2}$ for (**c**)]

While a positive $\langle \mathrm{M}\rangle'$ is generally in phase with an active BSISO convection, its tendency ($\langle \partial_t \mathrm{M}\rangle'$) exhibits a marked north–south asymmetry about the convection center, with positive (negative) anomalies to the north (south). Such a north–south asymmetry promotes the northward propagation of the BSISO convection, and is caused by various processes. Due mainly to the distinct background states, the role that a specific process plays in the $\langle \mathrm{M}\rangle'$ budget could have large spatial discrepancies, and could also change at different stages of a BSISO cycle. The regional and phase dependence of $\langle \mathrm{M}\rangle'$ budget is thus investigated by comparing the results over the WNP and BoB regions at the initiating and developing stages of a BSISO convection. General conclusions are illustrated in a schematic diagram (Fig. 16) and stated below.

The advection processes are the principal factors in generating the observed north–south asymmetry of $\langle \partial_t \mathrm{M}\rangle'$. As the BSISO rainband and positive $\langle \mathrm{M}\rangle'$ have a northwest-southeast tilted structure and the latter is maximized in the lower troposphere, the horizontal advection of anomalous

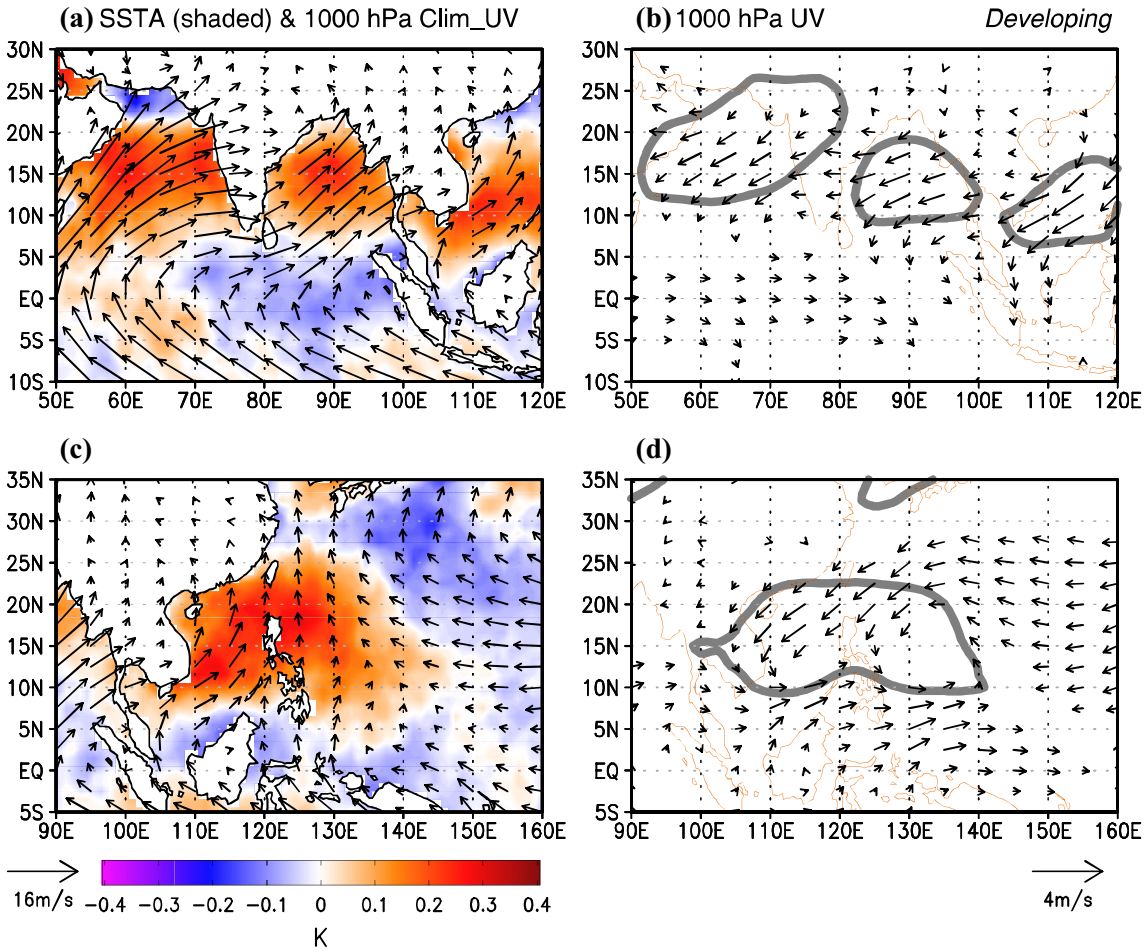

Fig. 14 **a** Intraseasonal SST anomalies (shaded) at the developing stage, and climatological JJA 1000 hPa winds over BoB. **b** Intraseasonal 1000 hPa circulation at the developing stage over BoB. **c**, **d** Are same as in (**a**), (**b**), but for WNP area. Thick contours indicate areas where $\partial_t\langle \mathrm{M}\rangle \geq 10\mathrm{W/m^2}$

MSE by the background low-level southwesterly monsoon flow plays the leading role (white arrows acting on the blue zones in Fig. 16). While the meridional advection dominates in most cases, the zonal advection is particularly important over the BoB at the developing stage, in the existence of strong background westerly and markedly tilted rainband. In addition, a much stronger subsidence appears to the north than the south of the convection when it is near the equator (purple downward arrows in Fig. 16), resulting in a greater vertical MSE advection to the north of the equator and supporting the initiation of the northward propagation. This is mainly caused by the equatorial asymmetry of the summer mean state, as a subsidence perturbation inhibits the more active background ascending to the north of the equator and forms a positive feedback through reduced diabatic heating.

The dominant external sources of $\langle \mathrm{M}\rangle'$, namely, the longwave radiative heating and surface upward latent heat flux generally reduce the observed north–south asymmetry of $\langle \partial_t \mathrm{M}\rangle'$ and thus hinder the northward propagation of BSISO. These two processes are related to intraseasonal vertical and horizontal motions, respectively. Vertically, while the strong subsidence to the north of the convection at the initiating stage induces a greater vertical MSE advection, it is partially offset by the enhanced outgoing longwave radiation, as there is less cloud cover over the subsidence area. Horizontally, the Rossby wave response to the BSISO convective heating produces an easterly (westerly) anomaly to the north (south) of the convection center (black arrows in Fig. 16), which is roughly in the opposite (same) direction of the background flow and thus decreases (increases) the near-surface wind speed. Such an intraseasonal near-surface wind speed distribution contributes to suppressed (enhanced) surface evaporation to the north (south) of the convection center, which goes against the observed north–south asymmetry of $\langle \partial_t \mathrm{M}\rangle'$.

Pronounced regional differences between WNP and BoB in the $\langle \mathrm{M}\rangle'$ budget have been detected, which is generally characterized by a more important role of zonal advection over the BoB than over the WNP, together with

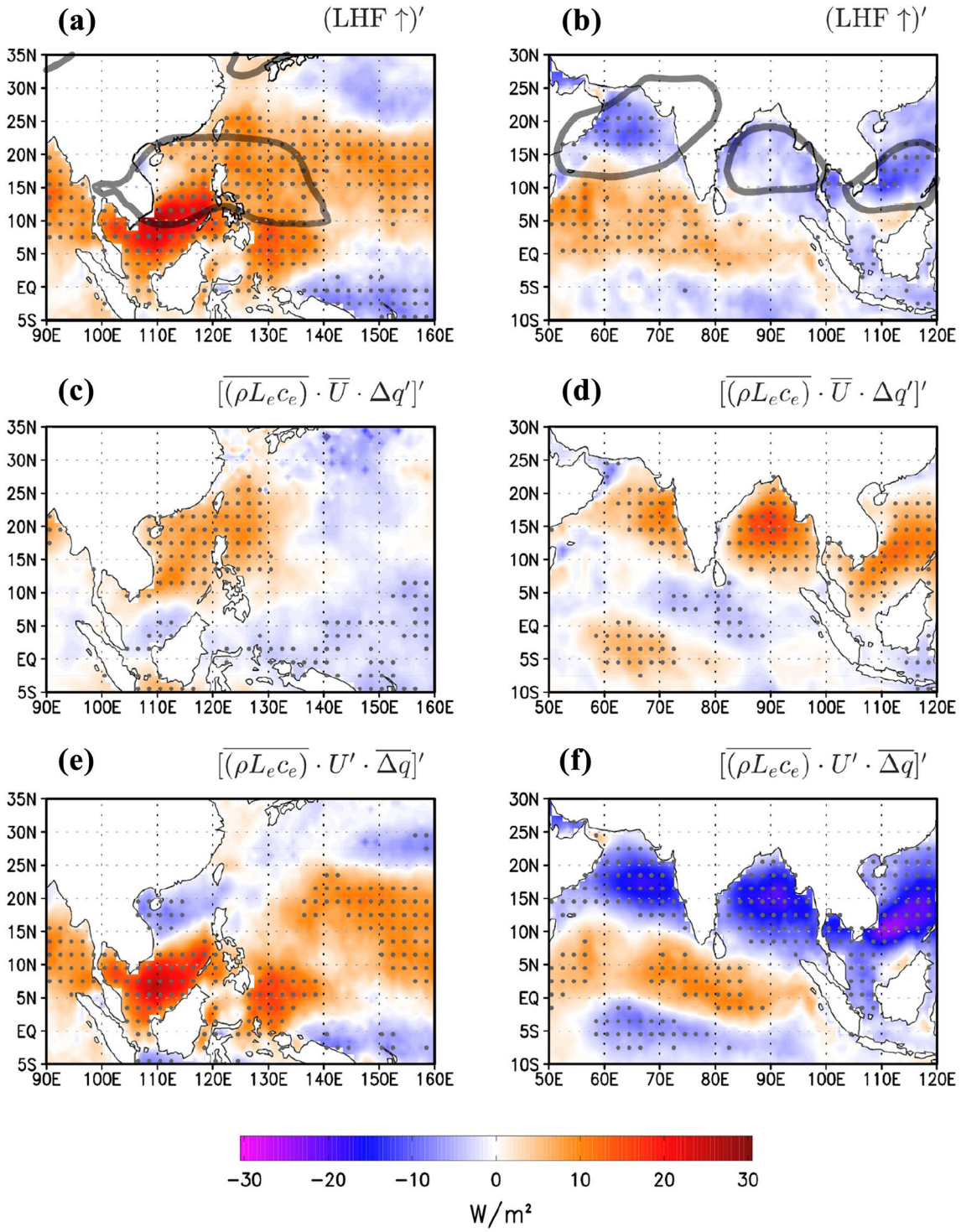

Fig. 15 Left panel: composite intraseasonal anomalies of **a** surface upward latent heat flux, and its **c** intraseasonal sea-air specific humidity difference related component, and **e** intraseasonal near-surface wind speed related component, at developing stage over the WNP area. Right panel: same as in the left panel, but for the BoB area. Dotted areas passed the significant test at the 90% level (Student's *t* test). Thick contours indicate areas where $\partial_t \langle \mathrm{M} \rangle \geq 10\ \mathrm{W/m^2}$

a positive contribution of surface evaporation over the WNP at the developing stage. The distinct land-sea distributions and background circulations are responsible for such regional differences. During boreal summer, the lower tropospheric MSE is maximized over the Asian land region due mainly to the thermal effect. As a result,

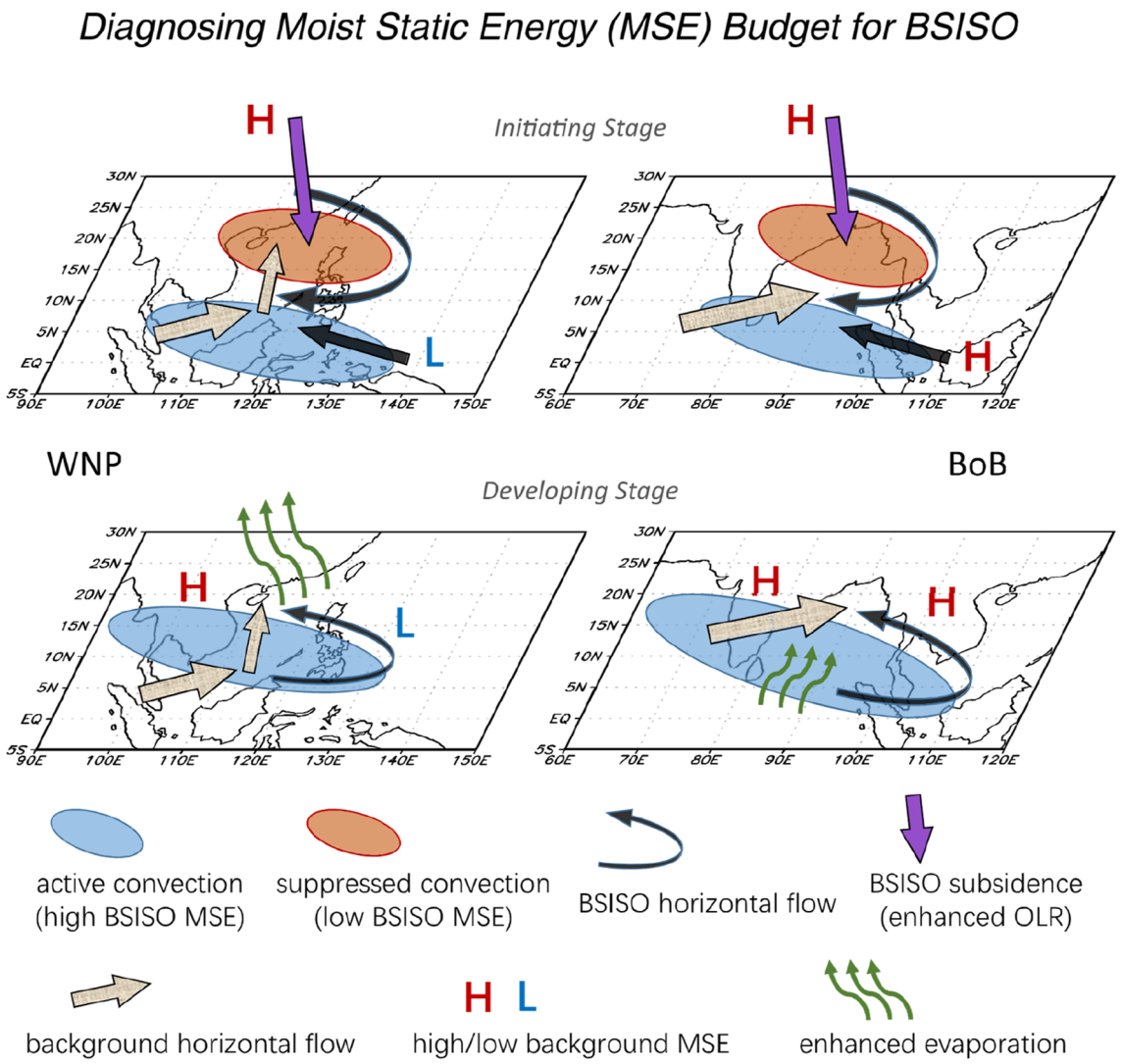

Fig. 16 Schematic diagram illustrating the principal processes in the column-integrated MSE budgets associated with the northward-propagating BSISO, for WNP (left panel) and BoB (right panel) areas at initiating (upper panel) and developing (lower panel) stages

the MSE advection by the easterly anomaly to the north of the BSISO convection contributes negatively over the WNP while it has little impact over the BoB. In addition, the prevailing low-level wind direction is southerly over the WNP but westerly over the BoB, leading to a differential advection of anomalous MSE. The prevailing southerly also results in a less impact of easterly anomaly on the near-surface wind speed change, so that the warm SST anomaly to the north of the convection contributes to an enhanced surface evaporation over the WNP at the developing stage. The warm SST anomaly is a delayed response forced by suppressed evaporation and enhanced insolation associated with the BSISO subsidence.

5.2 Discussion

From different aspects, two general features can be concluded from the current results of BSISO MSE budgets. One is while the advection processes are the principal factors in generating the observed north–south asymmetry of the MSE tendency, the external sources of the MSE that related to diabatic heating processes tend to inhibit it, as mentioned before. Another one is while the background southwesterly monsoon circulation contributes positively via horizontal advections, the anomalous BSISO wind contributes negatively to the north–south asymmetry of the MSE tendency. This is because the low-level easterly anomaly to the north

of the BSISO convection tends to suppress the surface evaporation through reducing near-surface wind speed, and the MSE advection by the easterly anomaly has weak impact or even contributes negatively.

The second conclusion above disagrees with those found in the eastward-propagating winter MJO (Kim et al. 2014; Sobel et al. 2014; Adames and Wallace 2015; Wang et al. 2017; Jiang 2017) and some of the previous studies on the northward-propagating BSISO (e.g., Adames et al. 2016; Jiang et al. 2018), as most of them emphasized the role of advection of background MSE by the intraseasonal circulation. Particularly, the zonal advection by the anomalous BSISO wind is suggested to be the fundamental cause of the northward propagation in Adames et al. (2016) and Jiang et al. (2018). However, the same term has relatively small impact or could even play negative roles in the current study.

We argue that the disagreements between the current work and previous studies on the northward-propagating BSISO mainly come from the regional and phase dependence of the MSE budgets. For instance, Jiang et al. (2018) focused on a broad region of the Indian Ocean, in which the Asian land with higher background MSE is located to the northeastern edge. In this case, an easterly anomaly to the north of the near-equator BSISO convection leads to a large positive background MSE advection. In our study, the analyzed areas are targeted to those with larger intraseasonal variabilities and pronounced northward propagations. The west portion of the Indian Ocean which has a higher background MSE to the east, however, is excluded. On the contrary, due to the distinct land-sea distribution, the background MSE has a weak zonal gradient over the BoB area, and has a lower (higher) value to the east (west) of the WNP area. Therefore, the MSE advection by the easterly anomaly plays a less important role in our study. Particularly, we point out that it hinders the northward propagation over the WNP.

The northwest–southeast tilted rainband is a striking feature of the northward-propagating BSISO. With such a structure, the large-scale BSISO appears to be propagating northeastward (Wang et al. 2006). Adames et al. (2016) suggested that while the anomalous easterly/westerly favors the northward propagation, the advection of anomalous moisture by the background westerly monsoon flow causes the eastward propagation. Here we point out that since the southerly component exists in the low-level monsoon circulation, particularly over the BoB and WNP where BSISO is more active, the MSE advection by background flow is crucial for the northward propagation. The role of the meridional MSE or PBL moisture advection induced by mean flow has also been reported in previous studies (Hsu and Weng 2001; Chou and Hsueh 2010; Demott et al. 2013; Wang et al. 2018; Gao et al. 2019). In addition, as long as the northwest-southeast tilted rainband is formed, the background westerly transports larger MSE anomaly over its northwest downstream, and favors a northward propagation of the southeastern portion of the rainband. This process could dominate the horizontal advections as revealed in Fig. 8d, during which a markedly tilted rainband is formed and background westerly is strong there. It is further speculated that once the northward propagation of a BSISO convection near the equator is initiated, for instance, supported by the vertical MSE advection by stronger subsidence anomaly to the north, the background southwesterly thus encourages the formation of a northwest-southeast tilted rainband and its northeastward propagation. Related issues will be explored in our future work.

Acknowledgements This work was jointly supported by China National Key R&D Program 2018YFC1505805, NSFC Grants 41575043/41875069, NSF AGS-1643297, and NOAA NA18OAR4310298. This is SOEST contribution number 10922, IPRC contribution number 1434 and ESMC number 309.

References

Adames ÁF, Kim D (2016) The MJO as a dispersive, convectively coupled moisture wave: theory and observations. J Atmos Sci 73:913–941. https://doi.org/10.1175/JAS-D-15-0170.1

Adames ÁF, Wallace JM (2015) Three-dimensional structure and evolution of the moisture field in the MJO. J Atmos Sci 72:3733–3754. https://doi.org/10.1175/JAS-D-15-0003.1

Adames ÁF, Wallace JM, Monteiro JM (2016) Seasonality of the structure and propagation characteristics of the MJO. J Atmos Sci 73:3511–3526. https://doi.org/10.1175/JAS-D-15-0232.1

Bellon G, Sobel A (2008a) Poleward-propagating intraseasonal monsoon disturbances in an intermediate-complexity axisymmetric model. J Atmos Sci 65:470–489. https://doi.org/10.1175/2007JAS2339.1

Bellon G, Sobel A (2008b) Instability of the axisymmetric monsoon flow and intraseasonal oscillation. J Geophys Res 113:D7108. https://doi.org/10.1029/2007JD009291

Chen T, Chen J (1993) The 10–20-day mode of the 1979 Indian monsoon: its relation with the time variation of monsoon rainfall. Mon Weather Rev 121:2465–2482. https://doi.org/10.1175/1520-0493(1993)121%3C2465:TDMOTI%3E2.0.CO;2

Chou C, Hsueh Y (2010) Mechanisms of northward-propagating intraseasonal oscillation—a comparison between the indian ocean and the western north Pacific. J. Climate 23:6624–6640. https://doi.org/10.1175/2010JCLI3596.1

Cui J, Wang L, Li T, Wu B (2020) Can reanalysis products with only surface variables assimilated capture Madden–Julian oscillation characteristics? Int J Climatol 40:1279–1293. https://doi.org/10.1002/joc.6270

Demott CA, Stan C, Randall DA (2013) Northward propagation mechanisms of the boreal summer intraseasonal oscillation in the ERA-interim and SP-CCSM. J. Clim 26:1973–1992. https://doi.org/10.1175/JCLI-D-12-00191.1

Drbohlav HL, Wang B (2005) Mechanism of the northward-propagating intraseasonal oscillation: insights from a zonally symmetric model. J. Clim 18:952–972. https://doi.org/10.1175/JCLI3306.1

Fu X, Wang B, Li T, Mccreary JP (2003) Coupling between northward-propagating, intraseasonal oscillations and sea surface temperature in the Indian Ocean. J Atmos Sci 60:1733–1753. https://doi.org/10.1175/1520-0469(2003)060%3c1733:CBNIOA%3e2.0.CO;2

Fukutomi Y, Yasunari T (1999) 10–25 day intraseasonal variations of convection and circulation over East Asia and Western North Pacific during early summer. J Meteorol Soc Jpn 77:753–769

Gao Y, Klingaman NP, Demott CA, Hsu P (2019) Diagnosing Ocean feedbacks to the BSISO: SST-modulated surface fluxes and the moist static energy budget. J Geophys Res Atmos 124:146–170. https://doi.org/10.1029/2018JD029303

Hendon HH, Salby ML (1994) The life cycle of the Madden–Julian oscillation. J Atmos Sci 51:2225–2237. https://doi.org/10.1175/1520-0469(1994)051%3c2225:TLCOTM%3e2.0.CO;2

Hsu P, Li T (2012) Role of the boundary layer moisture asymmetry in causing the eastward propagation of the Madden–Julian oscillation. J. Clim 25:4914–4931. https://doi.org/10.1175/JCLI-D-11-00310.1

Hsu H, Weng C (2001) Northwestward propagation of the intraseasonal oscillation in the western north Pacific during the boreal summer: structure and mechanism. J. Clim 14:3834–3850. https://doi.org/10.1175/1520-0442(2001)014%3c3834:NPOTIO%3e2.0.CO;2

Jiang X (2017) Key processes for the eastward propagation of the Madden-Julian oscillation based on multimodel simulations. J Geophys Res Atmos 122:755–770. https://doi.org/10.1002/2016JD025955

Jiang X, Li T (2005) Reinitiation of the boreal summer intraseasonal oscillation in the tropical Indian Ocean. J. Clim 18:3777–3795. https://doi.org/10.1175/JCLI3516.1

Jiang X, Li T, Wang B (2004) Structures and mechanisms of the northward propagating boreal summer intraseasonal oscillation. J. Clim 17:1022–1039. https://doi.org/10.1175/1520-0442(2004)017%3c1022:SAMOTN%3e2.0.CO;2

Jiang X, Adames ÁF, Zhao M, Waliser D, Maloney E (2018) A unified moisture mode framework for seasonality of the Madden–Julian oscillation. J. Clim 31:4215–4224. https://doi.org/10.1175/JCLI-D-17-0671.1

Jones C, Carvalho LMV, Wayne Higgins R, Waliser DE, Schemm JE (2004) Climatology of tropical intraseasonal convective anomalies: 1979–2002. J. Climate 17:523–539. https://doi.org/10.1175/1520-0442(2004)017%3c0523:COTICA%3e2.0.CO;2

Kang I, Kim D, Kug J (2010) Mechanism for northward propagation of boreal summer intraseasonal oscillation: convective momentum transport. Geophys Res Lett 37:L24804. https://doi.org/10.1029/2010GL045072

Kemball-Cook S, Wang B (2001) Equatorial waves and air-sea interaction in the boreal summer intraseasonal oscillation. J. Climate 14:2923–2942. https://doi.org/10.1175/1520-0442(2001)014%3c2923:EWAASI%3e2.0.CO;2

Kikuchi K, Wang B, Kajikawa Y (2012) Bimodal representation of the tropical intraseasonal oscillation. Clim Dyn 38:1989–2000. https://doi.org/10.1007/s00382-011-1159-1

Kim D, Kug J, Sobel AH (2014) Propagating versus nonpropagating Madden–Julian oscillation events. J. Clim 27:111–125. https://doi.org/10.1175/JCLI-D-13-00084.1

Krishnamurti TN, Ardanuy P (1980) The 10–20-day westward propagating mode and "breaks in the monsoons". Tellus 32:15–26. https://doi.org/10.1111/j.2153-3490.1980.tb01717.x

Lau K, Chan PH (1986) Aspects of the 40–50 day oscillation during the northern summer as inferred from outgoing longwave radiation. Mon Weather Rev 114:1354–1367. https://doi.org/10.1175/1520-0493(1986)114%3c1354:AOTDOD%3e2.0.CO;2

Lawrence DM, Webster PJ (2002) The boreal summer intraseasonal oscillation: relationship between northward and eastward movement of convection. J Atmos Sci 59:1593–1606. https://doi.org/10.1175/1520-0469(2002)059%3c1593:TBSIOR%3e2.0.CO;2

Lee J, Wang B, Wheeler M, Fu X, Waliser D, Kang I (2013) Real-time multivariate indices for the boreal summer intraseasonal oscillation over the Asian summer monsoon region. Clim. Dynam. 40:493–509. https://doi.org/10.1007/s00382-012-1544-4

Li T (2014) Recent advance in understanding the dynamics of the Madden–Julian oscillation. J. Meteorol Res-Prc 28:1–33. https://doi.org/10.1007/s13351-014-3087-6

Li T, Wang B (2005) A review on the western North Pacific monsoon: synoptic-to-interannual variabilities. Terr Atmos Ocean Sci 2:285–314. https://doi.org/10.3319/TAO.2005.16.2.285(A)

Li T, Zhao C, Hsu P, Nasuno T (2015) MJO initiation processes over the tropical indian ocean during DYNAMO/CINDY2011. J. Clim 28:2121–2135. https://doi.org/10.1175/JCLI-D-14-00328.1

Li T et al (2018) A Paper on the tropical intraseasonal oscillation published in 1963 in a Chinese journal. B Am Meteorol Soc 99:1765–1779. https://doi.org/10.1175/BAMS-D-17-0216.1

Liebmann B, Smith CA (1996) Description of a complete (interpolated) outgoing longwave radiation dataset. Bull Am Meteorol Soc 77:1275–1277

Lin J, Mapes B, Zhang M, Newman M (2004) Stratiform precipitation, vertical heating profiles, and the Madden–Julian oscillation. J Atmos Sci 61:296–309. https://doi.org/10.1175/1520-0469(2004)061%3c0296:SPVHPA%3e2.0.CO;2

Liu F, Wang B, Kang I (2015) Roles of barotropic convective momentum transport in the intraseasonal oscillation. J. Clim 28:4908–4920. https://doi.org/10.1175/JCLI-D-14-00575.1

Madden RA (1986) Seasonal variations of the 40–50 day oscillation in the tropics. J Atmos Sci 43:3138–3158. https://doi.org/10.1175/1520-0469(1986)043%3c3138:SVOTDO%3e2.0.CO;2

Madden RA, Julian PR (1971) Detection of a 40–50 day oscillation in the zonal wind in the Tropical Pacific. J Atmos Sci 28:702–708. https://doi.org/10.1175/1520-0469(1971)028%3c0702:DOADOI%3e2.0.CO;2

Madden RA, Julian PR (1972) Description of global-scale circulation cells in the tropics with a 40–50 day period. J Atmos Sci 29:1109–1123. https://doi.org/10.1175/1520-0469(1972)029%3c1109:DOGSCC%3e2.0.CO;2

Madden RA, Julian PR (1994) Observations of the 40–50-day tropical oscillation—a review. Mon Weather Rev 122:814–837. https://doi.org/10.1175/1520-0493(1994)122%3c0814:OOTDTO%3e2.0.CO;2

Neelin JD, Held IM (1987) Modeling tropical convergence based on the moist static energy budget. Mon Weather Rev 115:3–12. https://doi.org/10.1175/1520-0493(1987)115%3c0003:MTCBOT%3e2.0.CO;2

Pillai PA, Sahai AK (2016) Moisture dynamics of the northward and eastward propagating boreal summer intraseasonal oscillations: possible role of tropical Indo–West Pacific SST and circulation. Clim Dyn 47:1335–1350. https://doi.org/10.1007/s00382-015-2904-7

Raymond DJ, Fuchs (2009) Moisture modes and the Madden–Julian oscillation. J. Climate 22:3031–3046. https://doi.org/10.1175/2008JCLI2739.1

Roxy M, Tanimoto Y (2012) Influence of sea surface temperature on the intraseasonal variability of the South China Sea summer monsoon. Clim Dyn 39:1209–1218. https://doi.org/10.1007/s00382-011-1118-x

Saha S et al (2010) The NCEP climate forecast system reanalysis. Bull Am Meteorol Soc 91:1015–1057. https://doi.org/10.1175/2010BAMS3001.1

Salby ML, Hendon HH (1994) Intraseasonal behavior of clouds, temperature, and motion in the tropics. J Atmos Sci 51:2207–2224. https://doi.org/10.1175/1520-0469(1994)051%3c2207:IBOCTA%3e2.0.CO;2

Sobel A, Maloney E (2012) An Idealized Semi-Empirical Framework for Modeling the Madden–Julian Oscillation. J Atmos Sci 69:1691–1705. https://doi.org/10.1175/JAS-D-11-0118.1

Sobel A, Maloney E (2013) Moisture Modes and the Eastward Propagation of the MJO. J Atmos Sci 70:187–192. https://doi.org/10.1175/JAS-D-12-0189.1

Sobel A, Wang S, Kim D (2014) Moist static energy budget of the MJO during Dynamo. J Atmos Sci 71:4276–4291. https://doi.org/10.1175/JAS-D-14-0052.1

Tsou C, Hsu P, Kau W, Hsu H (2005) Northward and northwestward propagation of 30–60 day oscillation in the tropical and extratropical western north Pacific. J Meteorol. Soc Jpn 83:711–726

Vecchi GA, Harrison DE (2002) Monsoon breaks and subseasonal sea surface temperature variability in the Bay of Bengal. J. Clim 15:1485–1493. https://doi.org/10.1175/1520-0442(2002)015%3c1485:MBASSS%3e2.0.CO;2

Wang B, Li T (1994) Convective Interaction with boundary-layer dynamics in the development of a tropical intraseasonal system. J Atmos Sci 51:1386–1400. https://doi.org/10.1175/1520-0469(1994)051%3c1386:CIWBLD%3e2.0.CO;2

Wang L, Li T (2020) Effect of vertical moist static energy advection on MJO eastward propagation: sensitivity to analysis domain. Clim Dyn 54:2029–2039. https://doi.org/10.1007/s00382-019-05101-8

Wang B, Rui H (1990) Synoptic climatology of transient tropical intraseasonal convection anomalies: 1975–1985. Meteorol Atmos Phys 44:43–61. https://doi.org/10.1007/BF01026810

Wang B, Xie X (1996) Low-frequency equatorial waves in vertically sheared zonal flow. Part I: stable waves. J Atmos Sci 53:449–467. https://doi.org/10.1175/1520-0469(1996)053%3c0449:LFEWIV%3e2.0.CO;2

Wang B, Wu R, Li T (2003) Atmosphere-warm ocean interaction and its impacts on Asian–Australian monsoon variation. J Clim 16:1195–1211. https://doi.org/10.1175/1520-0442(2003)16%3c1195:AOIAII%3e2.0.CO;2

Wang B, Webster P, Kikuchi K, Yasunari T, Qi Y (2006) Boreal summer quasi-monthly oscillation in the global tropics. Clim Dyn 27:661–675. https://doi.org/10.1007/s00382-006-0163-3

Wang L, Li T, Maloney E, Wang B (2017) Fundamental causes of propagating and nonpropagating MJOs in MJOTF/GASS models. J Clim 30:3743–3769. https://doi.org/10.1175/JCLI-D-16-0765.1

Wang T, Yang X, Fang J, Sun X, Ren X (2018) Role of air-sea interaction in the 30–60-day boreal summer intraseasonal oscillation over the western north Pacific. J Clim 31:1653–1680. https://doi.org/10.1175/JCLI-D-17-0109.1

Xie X, Wang B (1996) Low-frequency equatorial waves in vertically sheared zonal flow. Part II: unstable waves. J Atmos Sci 53:3589–3605. https://doi.org/10.1175/1520-0469(1996)053%3c3589:LFEWIV%3e2.0.CO;2

Yasunari T (1979) Cloudiness fluctuations associated with the northern hemisphere summer monsoon. J Meteorol Soc Jpn 57:227–242

Yu L, Weller RA (2007) Objectively analyzed air-sea heat fluxes for the global ice-free oceans (1981–2005). Butt Am Meteorol Soc 88:527–539. https://doi.org/10.1175/BAMS-88-4-527

Yu L, Jin X, Weller RA (2008) Multidecade global flux datasets from the objectively analyzed air-sea fluxes (OAFlux) project: latent and sensible heat fluxes, ocean evaporation, and related surface meteorological variables. OAFlux Project Technical Report (OA-2008-01), 3 ed., Woods Hole Oceanographic Institution

Zhang C, Dong M (2004) Seasonality in the Madden–Julian oscillation. J. Climate 17:3169–3180. https://doi.org/10.1175/1520-0442(2004)017%3c3169:SITMO%3e2.0.CO;2

Zhao C, Li T, Zhou T (2013) Precursor signals and processes associated with MJO initiation over the tropical Indian Ocean. J Clim 26:291–307. https://doi.org/10.1175/JCLI-D-12-00113.1